Master thesis : Feasibility Study of a Mid-wave Infrared CubeSat for Smart Irrigation of Agricultural Fields - "OUFTI-NEXT"

Auteur : Ghidoli, Enrico
Promoteur(s) : Kerschen, Gaetan
Faculté : Faculté des Sciences appliquées
Diplôme : Cours supplémentaires destinés aux étudiants d'échange (Erasmus, ...)
Année académique : 2016-2017
URI/URL : http://hdl.handle.net/2268.2/2566

Université de Liège - Faculty of Applied Sciences

Feasibility Study of a Mid-wave Infrared CubeSat for Smart Irrigation of Agricultural Fields

OUFTI-NEXT

Author:
E. Ghidoli

Supervisor:
Prof. G. Kerschen

Co-Supervisor:
Prof. S. Habraken

Graduation Studies conducted for obtaining the Master's degree in Aerospace Engineering

Academic Year 2016 – 2017

Abstract

OUFTI-NEXT is going to be the third CubeSat developed by Université de Liège. It is expected to be one of the first CubeSats equipped with a Mid-Wave Infrared camera and the first demonstrator for the use of this technology for agricultural fields temperature monitoring.

This work has the aim to evaluate if the required performances can be reached by a 3U CubeSat orbiting in LEO and then, if the OUFTI-NEXT mission is feasible. To answer that question, the necessary instrument characteristics have been individualized and compared with commercially available cameras.

To evaluate the feasibility of the mission, a software for study how the different parameters influence the instrument performances has been developed. In particular, a procedure for a quick evaluation of the thermal resolution has been realized. Models for radiometry, optics, and detector to be implemented in parametric studies are going to be proposed.

Keywords: *CubeSat, OUFTI-NEXT, MWIR, Feasibility Study, Radiometry, Thermal Imaging.*

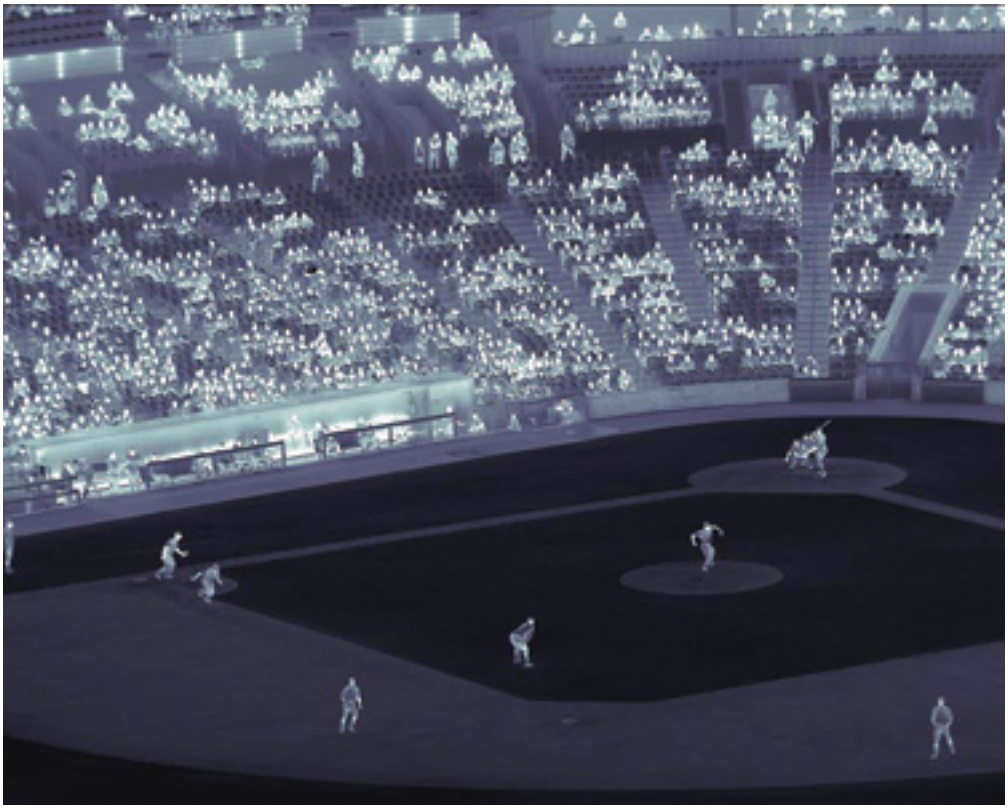

Figure 1: A mid-wave IR nBn focal-plane array (FPA) with 1280 × 1024 pixels images a scene from a baseball game, with a player attempting to steal second base. From: *Arn Adams and Elliott Rittenberg: "Advances in detectors: HOT IR sensors improve IR camera size, weight, and power", Laser Focus World, January 7th 2014*

Acknowledgements

First of all, I wish to thank my supervisor Prof. Gaëtan Kerschen, co-supervisor Prof. Serge Habraken, and Prof. Jerôme Loicq for them continuous support and willingness. They believed in my ability to face a subject in which I had no any previous experience and put me always in the first line in the development of this amazing project, making me feel an integral part of it. Thanks to them and to the rest of the team, Ing. Xavier Werner and Dimitry Schklar, that job has been a great professional experience. I'm grateful to Ing. Lucas Salvador for being my first contact in the CSL and allowing my work there.

I would like to express my gratitude to my supervisor at Politecnico di Milano, Prof. James Douglas Biggs, for encouraging me before my departure and has always been available despite the distance during the whole work.

My special thanks to Ivan, Monica, Chris, Pedro, Pablo, João, Aida, Marco, Veronika, Tibor, and all the other Erasmus students for made this exchange in Liège unforgettable.

Thanks to Lorenzo, Mathieu, Niccolò, Gianluca, Francesco, Maria, Alessio, Giacomo, Rocco, Raouf, and the other future Aerospatial Engineers that for five years have shared the passion and the effort that our studies require.

Then, I'm thankful to my friends, the components of my rock band, and my rugby teammates, for continuously kept in touch during these months, always encouraging me and made me feel close to home. In particular, thanks to Daniele, Joel, Leonardo, Gabriele, Alessandro, Luca, Bruno, Andrea, Edoardo, Giovanni, Milena, Luca, Marco, Oriana, Luna, and Elisa.

I would also like to thanks all my relatives, in particular, my grandparents, Gregorio, Concetta, Enrico, and Giuditta, for be, and being, my best fans.

I wish to express my love and gratitude to Giuliana, for be my best side, for always be close to me despite the difficulties, and give me the force to never back down.

I'm grateful for my parents, Franco and Isabella, that always believe in me, that are my models, teaching me to do all my best, and that made it possible for me to follow my dream and build my own path. Without you, this would not have been possible.

And finally, thanks to my brother Gregorio and my sister Anna, for taking care of our parents during my absence, and always be on my side.

Liège, June, 2017

Contents

List of Figures

List of Tables

List of Symbols

ΔE	Bandgap Activation Energy	$[J]$
ΔT	Thermal Resolution	$[K]$
λ	Wavelegth	$[mum]$
μ_e	Earth Gravitational Parameter	$[km^3/s^2]$
Ω_{OD}	Optics Solid Angle	$[sr]$
$\Omega_{S,E}$	Solid Angle Coming from the Sun to the Earth	$[sr]$
ρ_g	Ground Reflection Coefficient	$[-]$
τ_a	Atmosphere Transmission Coefficient	$[-]$
$\theta_{1/2}$	Half Cone Angle	$[rad]$
ε_g	Ground Grey Body Emissivity	$[-]$
a	Orbit semi-major axis	$[km]$
A_d	Detector Area	$[m^2]$
A_p	Pupil Area	$[m^2]$
c	Velocity of Light	$[m/s]$
D	Pupil Diameter	$[mm]$
D_l	Diffraction Limit	$[\mu m]$
F	Flux at the Pupil	$[e^-/s]$
f	Focal Distance	$[mm]$
$f/\#$	f-number	$[-]$
H	Orbit Altitude	$[km]$
h	Planck's Constant	$[J\,s]$
I	Integrated Radiance along the observed Bandwidth	$[W/(m^2\,sr)]$
I_{DC}	Dark Current	$[A]$
I_{pupil}	Radiance at the Pupil	$[W/(m^2\,sr)]$
I_{tot}	Total Integrated radiance that reach the Spacecraft	$[W/(m^2\,sr)]$
k	Boltzman's Constant	$[J/K]$

L_s	Solar Emitted Spectral Radiance	$[W/(m^2\,sr\,m)]$
L_{emit}	Thermal Emitted Radiance from Ground	$[W/(m^2\,sr\,m)]$
$L_{exo\,atm}$	Exo Atmospheric Sun Radiance	$[W/(m^2\,m)]$
$L_{out,emit}$	Thermal Emitted Radiance after Atmosphere	$[W/(m^2\,sr\,m)]$
$L_{out,ref}$	Reflected Solar Radiance after Atmosphere	$[W/(m^2\,sr\,m)]$
N	Total Noise	$[e^-]$
N_S	Noise Signal	$[e^-]$
N_{bit}	Quantized Noise	$[e^-]$
n_{bit}	Digital Resolution	$[-]$
N_{DC}	Dark Current Noise	$[e^-]$
$N_{q\%}$	Noise-quantization rate	$[-]$
N_{RO}	Read Out Noise	$[e^-]$
P	Power at the Pupil	$[W]$
ps	Pixel Size	$[\mu m]$
q	Quantization Signal Step	$[e^-]$
Q_e	Electron's Charge	$[C]$
R_e	Earth's Radius	$[km]$
R_s	Sun Radius	$[m]$
S	Signal	$[e^-]$
S_{bit}	Quantized Signal	$[e-]$
S_{max}	Well Capacity	$[e^-]$
SW	Swadth	$[km]$
T_d	Detector Temperature	$[K]$
T_g	Ground Temperature	$[K]$
T_i	Integration Time	$[s]$
T_o	Orbital Period	$[s]$
T_s	Solar Temperature	$[K]$
T_{bit}	Quantized Temperature	$[K]$
T_{step}	Quantized Temperature Step	$[K]$
TF	Transmission coeff. of Linear Filter	$[-]$
V_{sat}	Satellite Velocity w.r.t. Ground	$[km/s]$

Acronyms

LWIR Long-Wave Infrared

MWIR Mid-Wave Infrared

NIRST New Infrared Sensor Technology

CIRAS CubeSat Infrared Atmospheric Sounder

HOT-BIRD High Operating Temperature Barrier Infrared Detector

MGS MWIR Grating Spectrometer

TET-1 Technology Experiment Carrier

BIRD Bi-spectral Infrared Detection

HSRS Hot Spot Recognition System

LEO Low Earth Orbit

GSD Ground Sample Distance

SNR Signal to Noise Ratio

NIR Near Infrared

SWIR Short-Wave Infrared

TMA Three Mirror Anistigmat

CCD Charge Coupled Device

RO Read Out

DC Dark Current

FOV Field Of View

iFOV Istantaneus Field Of View

TDI Time Delay Integration

AOCS Attitude and Orbit Control System

CSL Centre Spatial de Liège

FPA Focal Plane Array

Chapter 1

Introduction

Nowadays Earth observation missions are very common, especially in Visible and Long-Wave Infrared (LWIR) bandwidths. The first one is trivially related to Sunlight reflection while the second is suitable for obtain thermal information. Between these two extrems, other observable windows exist, in particular, the Mid-Wave Infrared (MWIR) bandwidth. In the MWIR window, which goes from 3μm to 5μm, both the Sun-reflected and Thermal Emitted radiances are present. Thanks to technology improvements it is now possible to exploit those wavelengths and their advantages.

1.1 Past Missions

The use of IR thermal imaging leads to the possibility of acquiring information about the target thermal state and its chemical composition leaving a large freedom in the final user purpose. For instance, the IR imaging can be used for atmosphere's temperature profiles determination, for gas species concentration (e.g. CO_2) identification, for geological/hydric monitoring, or for fire detection.

At the moment, only a few missions have been imagined to observe the MWIR window and the majority are still waiting to be launched (Tab.1.1).

ASC-D was a NASA mission carrying as secondary payload New Infrared Sensor Technology (NIRST) which used Microbolometer detector. Microbolometer is a family of uncooled sensors, this characteristic makes the system light and compact but sensitive only to high target's temperature variations. In fact, it has been used for fire detection purpose [1].

Arkyd-6 missions are developed by *Planetary Resource* to begin the demonstrators of the core technology to measure resources on water-rich asteroids. Included in the payload is a MWIR imaging system, able to precisely measure temperature differences of the objects it observes, as well as acquire key data related to the presence of water and water-bearing minerals. The system will first test targeted areas of our own planet before being deployed to near-Earth asteroids on future missions [2].

The Arkyd-100, also developed by *Planetary Resource*, will provide the company with the core spacecraft technologies necessary for asteroid prospecting while creating the first space telescope within reach of the private citizen. The Arkyd-100 contains the critical structures, avionics, attitude determination and control, and

Table 1.1: MWIR actual missions

NAME	**STATE**	**SENSOR**	**BAND** (μm)	**ORBIT** (km)	**GSD** (m)	**ACC.** (K)	**DIM.**
SAC-D	CONCL. (2011-2015)	512x2 Microbolometer (Uncooled)	3.4-4.2 (Lens)	657 (SSO)	351	2.5@400	⌀2.7x5m
ARKYD-6	N.L. (12-2017)	640X512 InSb (Cooled @77K)	3.4-5.1 (Lens)	N.A.	>30	N.A.	6U
ARKYD-100	N.L. (12-2017)	640X512 InSb (Cooled @77K)	3.4-5.1 (Mirror)	550 (SSO)	15	N.A.	12U
CIRAS	N.L. (2019)	504X625 HOT-BIRD (Cooled @120K)	4.78-5.09 (Lens)	400-800 (SSO)	13500	0.2@280	6U
TET-1	OPER. (2012)	512X1 CdHgTe (Cooled @90K)	3.4-4.2 (Lens)	500 (SSO)	178	1.85@285	67x58x88cm

instrumentation that enable low-cost asteroid exploration, which will be the target of the next Arkyd series [3].

The CubeSat Infrared Atmospheric Sounder (CIRAS) will measure upwelling infrared radiation of the Earth in the MWIR region of the spectrum from space on a CubeSat. The observed radiances have information of potential value to weather forecasting agencies and can be used to retrieve lower tropospheric temperature and water vapor globally for weather and climate science investigations. CIRAS incorporates key new instrument technologies including a 2D array of High Operating Temperature Barrier Infrared Detector (HOT-BIRD) material, selected for its high uniformity, low cost, low noise and higher operating temperatures than traditional materials. The detector is cooled to 120K also using a Ricor cryocooler, heat sunk to the warm radiator. Electronics, cryocooler and spacecraft waste heat is dissipated in warm temperature radiators on all remaining surfaces except nadir and anti-nadir.
The second key technology is an MWIR Grating Spectrometer (MGS) designed to provide imaging spectroscopy for atmospheric sounding in a CubeSat volume. The MGS has no moving parts and includes an immersion grating to reduce the volume and reduce distortion.
The third key technology is an infrared blackbody fabricated with black silicon to have very high emissivity in a flat plate construction [4].

The Technology Experiment Carrier (TET-1) went into orbit on 22 July 2012. Its design was based on its predecessor Bi-spectral Infrared Detection (BIRD), which was the first orbiter to be used in a small satellite mission for collecting data regard-

ing high-temperature events.
The initial objective of TET-1 was to carry out 11 experiments over the course of one year as part of the OOV program (On-Orbit Verification of new techniques and technologies). Together with BIROS it is part of the FireBIRD mission. TET-1's main payload is the high-performance infrared camera system known as the Hot Spot Recognition System (HSRS), which was already successfully used prior to the launch of BIROS as a forest fire detector. For example, in the summer of 2015, it was able to register and measure a large fire as well as several smaller fires in the US state of Oregon. In October 2015, the DLR satellite provided accurate images of the wide-spread forest and peat fires in Indonesia. Together with BIROS, as part of their joint FireBIRD mission, it has been in orbit since June 2016 [5].

1.2 OUFTI-NEXT

Students and professors of the *Université de Liège* (Belgium) are active in the development of CubeSats. In the list there are OUFTI-1 (Orbital Utility For Telecommunication Innovations), launched in 2016[1], OUFTI-2, still under development[2], and finally what is expected to be OUFTI-NEXT (Orbital Utility For Thermal Imaging) [3]. OUFTI-NEXT is under development in collaboration with the Centre Spatial de Liège (CSL).

The primary goal of the OUFTI-NEXT mission is intended to be perform Earth observation in MWIR band from a 3U CubeSat flying in a Low Earth Orbit (LEO). Then, use the acquired thermal information for agriculture purposes, focusing on the cultivated fields.

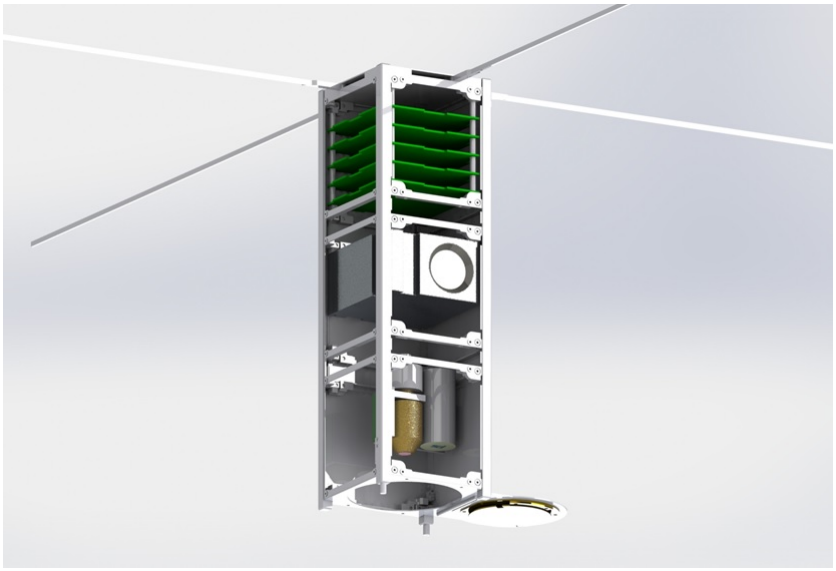

Figure 1.1: Expected aspect of OUFTI-NEXT 3U CubeSat

[1]Unfortunately, contact with OUFTTI-1 has been lost only after few seconds.
[2]OUFTI-2 will retry to test the main payload of OUFTI-1, plus other secondaries.
[3]This denomination is still not official.

To obtain suitable information the instrumentation must be able to look at the ground with a Ground Sample Distance (GSD) lower than 100m, detect temperature variations in the order of 1K, and with the higher as possible Signal to Noise Ratio (SNR). Moreover, the target is to contain the payload in 1.5U.
In order to evaluate the feasibility of the mission, a parametric preliminary study is necessary to know how orbit altitude, sensor, and optical system specifications influence the ground observation. Successively, it will be possible to select the appropriate instrument.

1.3 Methods

The aim of this work has been performing a parametric study to evaluate first how all the variables of the problem are linked with the required specifications (GSD, SNR etc...) and then the feasibility of the mission.

The first step has been model the Sun Reflected and Thermal Emitted Radiances that compound the radiometric budget. After that, individualize what characterize the optical system and the detector and apply the appropriate constraints. These constraints are substantially given by the instruments availability on the market (e.g. optics dimension, sensor array size etc..), since all the hardware components will be acquired externally and (if necessary) space qualified.
Obviously, the market offers several solutions. Hence, some variables are not strictly fixed but it is possible to limit them only at few values (e.g. the pixel size).

The problem has been modeled in separate sections:

- Radiometric budget (MWIR window, Sunlight, Thermal Emission etc...)
- Optical system (Pupil Diameter, Diffraction Limit etc...)
- Detector system (Array Dimension, Dark Current etc...)

A *Matlab* code has been developed to join all the different parts and equations to perform the parametric studies for the GSD and the SNR. Then, after evaluated their trends, simulations to predict the instrument requirements have been performed looking for a good balance between the two quantities.
After a research, the most promising hardware have been selected between what is offered by the different suppliers (basing on the results of the parametric studies). At this point, the data of the selected candidates have been used as the input variables in the code to simulate and verify the instruments performances.

Chapter 2

Models

2.1 Radiance

To predict the radiometric budget in the MWIR window, first of all, it is necessary to model the atmospheric transmission window. Then, the Sun Reflected and the Ground Thermal Emitted radiances can be evaluated.
Despite the reflected light coming from the Sun is largely lower in the MWIR than in the Visible window, it is still comparable with the amount of Ground Thermal Emitted radiance. What is supposed to reach the pupil of the satellite is a sum of the two effect.
Scattering, reflected downwelling for both solar and thermal radiances, and aerosol effects have been neglected at this stage. Moreover, condition of perfect clear sky has been considered. Hence, the results correspond to the most optimistic possible case.

2.1.1 MWIR Atmospheric Window

Due to the several gas species present in the atmosphere in different percentages, the atmosphere's transmission feature is very articulated along the spectrum (Fig.2.1). Despite the atmospherical absorption, it is possible to individualize some windows in which the transmission coefficient is high enough and almost constant (Fig.2.2):

- The Visible window, from 0.3 to 0.7 μm
- The Near Infrared (NIR) window, from 0.75 to 1 μm
- The Short-Wave Infrared (SWIR) window, from 1 to 2.7 μm
- The MWIR window, from 3 to 5 μm
- The LWIR window, from 8 to 14 μm

In this mission, observations are intended to be performed in MWIR window. Typically, at MWIR wavelengths, the radiative flux is impacted by the absorption by well-mixed gases such as Ozone (O_3), Oxygen (O_2), Nitrogen (N_2), Methane (CH_4), Nitrous Oxide (N_2O), Nitrogen Dioxide (NO_2) and Carbon Dioxide (CO_2), and the absorption by water vapor [6].
Water vapor is the major absorber in the MWIR and provides the bulk of the total atmospheric absorption. Since the amount of water vapor in the atmosphere varies greatly both spatially and temporally, its effect on transmission in the MWIR can also vary. Two major H_2O absorption bands are found in the MWIR: a strong

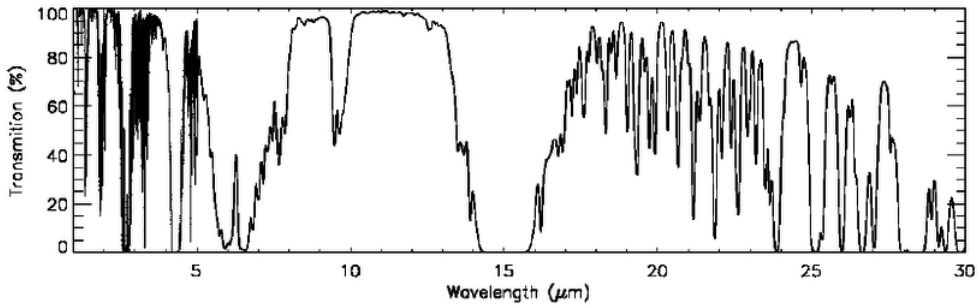

Figure 2.1: Atmospherical transmission coefficient [7]

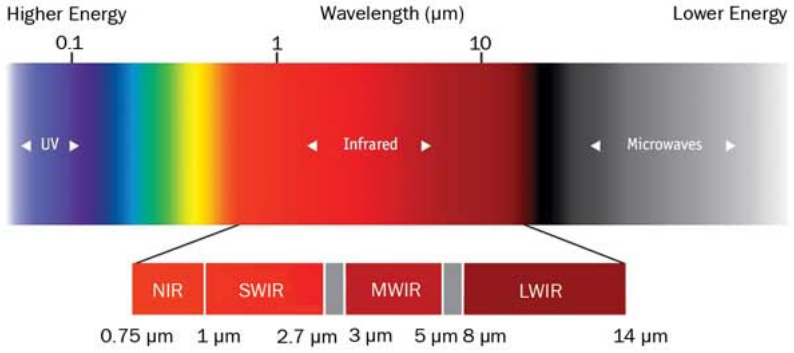

Figure 2.2: IR Atmospheric Windows

band near 2.7 μm and the major water vapor complex of lines near 6.7 μm. The latter band spans over 3 μm from 5 to 8 μm and represents a primary region of the spectrum for obtaining information used to retrieve layered atmospheric water vapor amounts. It can be seen that the water vapor absorption overwhelms weaker absorption by other gases, even for relatively dry atmospheres.

Carbon dioxide absorbs strongly between 4.1 and 4.4 μm and also near 2.8 μm. The 2.7 μm H2O absorption mostly eclipses the latter CO_2 band. CO_2 also exhibits a moderate absorption line at 4.85 and 5.2 μm; the effects of both are diminished by water vapor. Absorption by CO_2 at 4.25 μm is strong enough to provide the opportunity to estimate atmospheric temperatures in the Stratosphere using retrieval algorithms. Adjacent to this CO_2 band is a strong N_2O absorption band centered at 4.5 μm. Weaker bands are also found at 2.9, 3.9 and 4.05 μm, but only the 3.9 μm band falls within the MWIR window. Molecular nitrogen also displays a broad area of moderate absorption at 4.3 μm, the effect being to broaden the CO_2 absorption region to 3.9 μm. A moderate CH_4 absorption band is located near 3.3 μm on the edge of the water vapor band and extending into the MWIR window. Minor O3 absorption is present at 4.75 μm; CO displays minor absorption from 4.5 to 4.9 μm. Other gases, such as O_2, NO_2 and HNO_3 as well as CH_4 and O_3 display absorption from 5.5 to 7 μm, but the effects are completely encompassed by the expansive water vapor band [8].

Since this is going to be a preliminary study, the feature of the transmission coefficient ($\tau_a(\lambda)$) from 3 to 5 μm has been modeled in order to simplify the computations (Fig.2.3).

$$\tau_a(\lambda) = \begin{cases} 1.125\lambda - 3.375 & \text{if } 3 \leq \lambda \leq 3.4\,\mu m \\ 0.75 & \text{if } 3.4 < \lambda < 4.2\,\mu m \\ 0 & \text{if } 4.2 \leq \lambda \leq 4.4\,\mu m \\ -0.8871\lambda + 4.6129 & \text{if } 4.4 < \lambda \leq 5\,\mu m \end{cases} \tag{2.1}$$

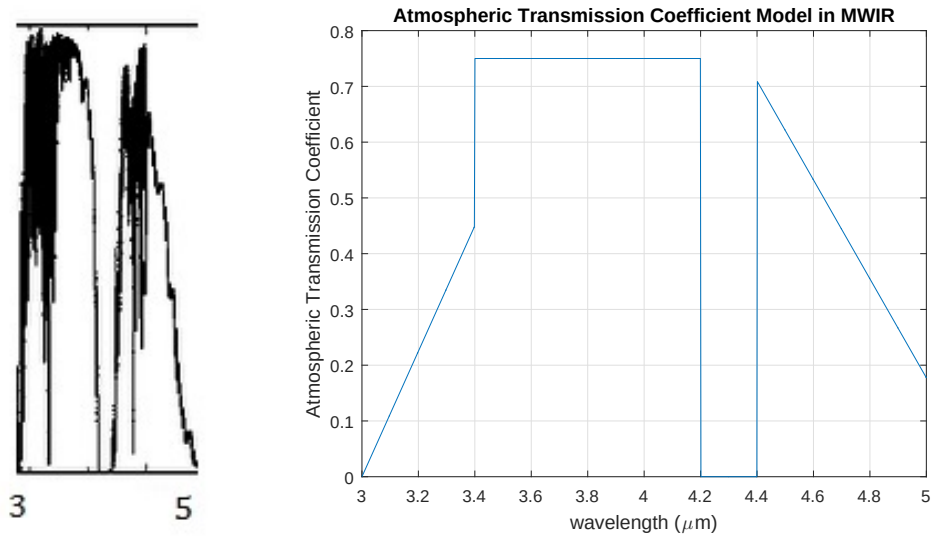

(a) **(b)**

Figure 2.3: MWIR Transmission Coefficient, (a)Real & (b)Model

2.1.2 Sun Reflected Component

With good approximation the Sun can be considered as a Black Body emitter at temperature $T_s = 5990K$ [9]. This lead to the possibility to compute the Solar Emitted Spectral Radiance $L_s(\lambda, T_s)$ by using the *Planck's equation* (Eq.2.2).

$$L_s(\lambda, T_s) = \frac{2hc^2}{\lambda^5(e^{\frac{hc}{\lambda k T_s}} - 1)} \tag{2.2}$$

Where $h = 6.62607004\,10^{-34}\,J\,s$ is the *Planck's constant*, $c = 3\,10^8\,m/s$ is the *Light Velocity*, $k = 1.38064852\,10^{-23}\,J/K$ is the *Boltzman's constant* and λ is the radiation wavelength. It is then possible to draw the spectral emissivity for the Sun (Fig.2.4). $L_s(\lambda, T_s)$ is the amount of power emitted along the spectrum, for the unit area, for steradians. To better understand it, it is useful to image that the Sun is emitting power at all the wavelengths with different intensities. This power can be assumed to be spread homogeneously by the whole surface defining a kind of power density for source's surface area. Finally, the distance between the observer and the source has to be considered. Assume that the Sun is an isotropic emitter in the space and that the power is propagating as a sphere. The sphere radius, as consequence, is equal to the distance from the source. This spatial distribution can be represented by a solid angle.

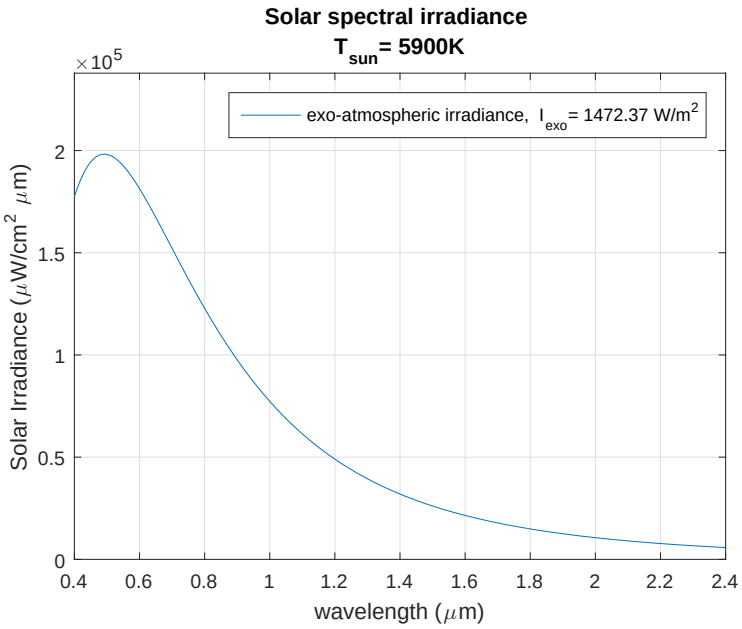

Figure 2.4: Solar Emitted Spectral Radiance

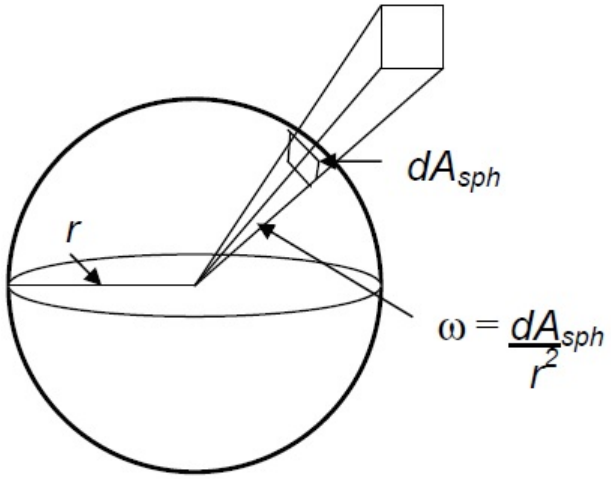

Figure 2.5: Solid Angle definition [10]

A Stearadian is defined as *the solid angle that, having its vertex in the center of a sphere, cuts off an area of the surface of the sphere equal to that of a square with sides of length equal to the radius of the sphere* [11](Fig.2.5).

The element of the solid angle subtended by the surface element dA_{sph} of a sphere of radius r, is expressed by:

$$d\omega = \frac{dA_{sph}}{r^2} \tag{2.3}$$

The distance between the Earth and the Sun is high enough to consider the Sun as a point source. Then, the irradiance which is supposed to reach the Earth $L_{exo\,atm}(\lambda, T_s)$ can be determined with a simple expression of the solid angle $\Omega_{S,E}$ coming out from the Sun to the Earth.

$$\Omega_{S,E} = 4\pi sin(\theta_{1/2})^2 \tag{2.4}$$

$$sin(\theta_{1/2})^2 = \frac{a^2}{a^2 + b^2} \tag{2.5}$$

$$L_{exo\,atm}(\lambda) = L_s(\lambda)\,\Omega_{S,E} \tag{2.6}$$

Where a is the Sun radius $R_s = 7\,10^8\,m$ and b is the Sun-Earth distance assumed to be constant and equal to $1.5\,10^{11}\,m$ (Fig.2.6).

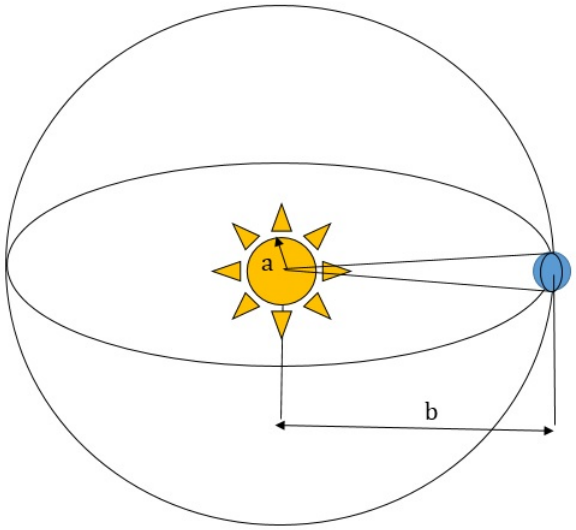

Figure 2.6: Representation of the Solid Angle exiting from the Sun center to the Earth, assuming that the Sun is a point source

For this study, the Sunlight has been considered to act normally to the ground. In other words, the Sun is always at the nadir with respect the ground and the angle variations during the day are not considered.
At this point, the amount of irradiance that reaches the Earth is known. Before reach the ground, part of the Sunlight is absorbed by the atmosphere. The absorption due to the atmosphere can be considered applying the transmission coefficient $\tau_a(\lambda)$ (Eq.2.1).

The irradiance that reaches the ground is in part absorbed and in part reflected. To evaluate the amount of reflected light, it is necessary to define the ground reflection coefficient (ρ_g). This coefficient is not easy to predict. In fact, it strongly depends on the ground composition and the radiation's wavelength. As in first approximation, a constant value along the MWIR window has been chose. In particular, a value of $\rho_g = 0.05$ has been arbitrarly assumed as an average for a generic ground (Fig.2.7).

Assuming that the Sunlight is reaching and leaving the Earth from one hemisphere, the reflected irradiance must be divided for a solid angle equal to $2\pi\, sr$[1]. Finally, considering also the second atmospherical absorption during the path from the ground to Space, the amount of Solar Reflected Radiance that reach the Spacecraft $L_{out,ref}$ can be estimated (Fig.2.8).

$$L_{out,ref}(\lambda) = \frac{L_{exo\,atm}(\lambda)}{2\,\pi}\,\tau_a(\lambda)^2\,\rho_g \tag{2.7}$$

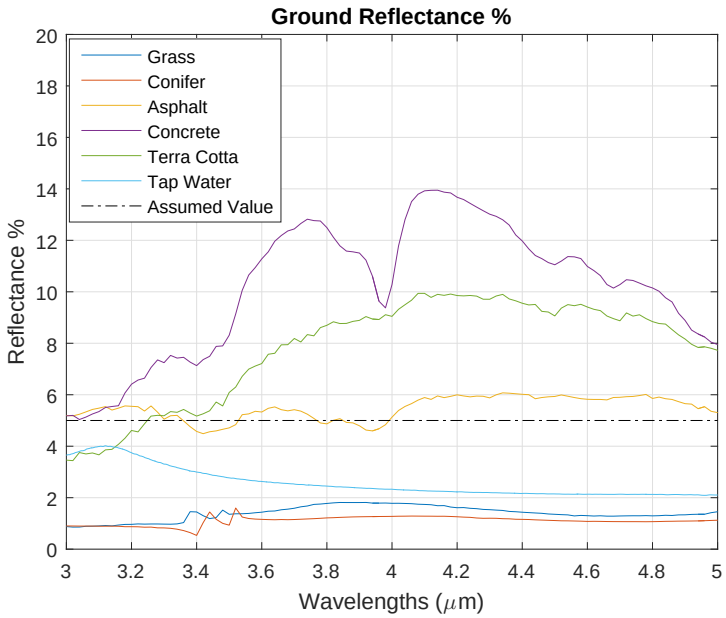

Figure 2.7: Reflectance coefficient for different ground compositions [12]

2.1.3 Ground Emitted Component

Green vegetation can completely cover a large surface. Based on their reflectance, the emittance from individual leaves and conifer needles is close to that of a black body in 3 to 5 μm region [13]. Since the main target are intended to be cultivated fields, where vegetation is usually not green and thick as in conifer woods, the hypothesis of black body emitter has been relaxed. Then, the ground has been modeled as a Grey Body Emitter of emissivity ε_g=0.8[2]. The ground temperature (T_g) is obviously variable and then, it will be necessary to perform simulations for several temperature values.

As for the Sun, the *Planck's curve* can be drawn.

$$L_{emit}(\lambda, T_g) = \frac{2hc^2}{\lambda^5(e^{\frac{hc}{\lambda k T_g}} - 1)}\,\varepsilon_g \tag{2.8}$$

[1] $\omega = 2\pi\, sr$ corresponds to one hemisphere solid angle
[2] ε_g=0.8 has been chosen arbitrarly

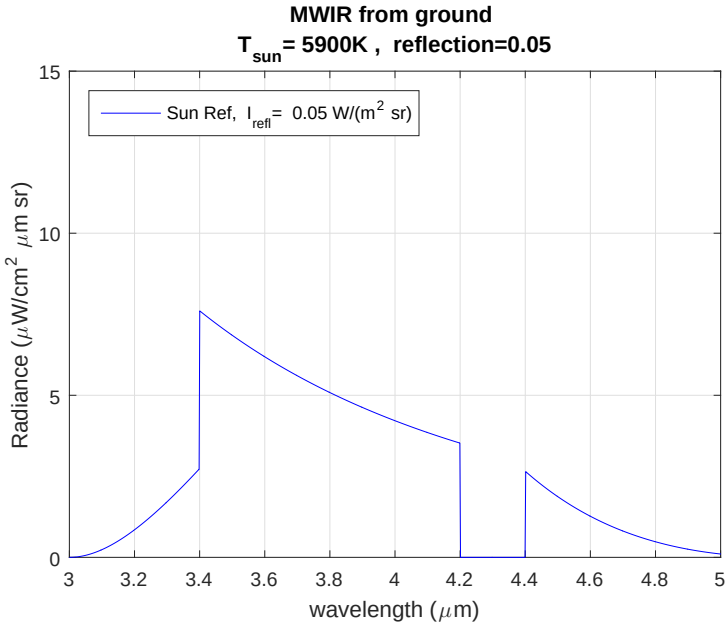

Figure 2.8: Sun Irradiance reflected by the ground after the second atmospherical absorption

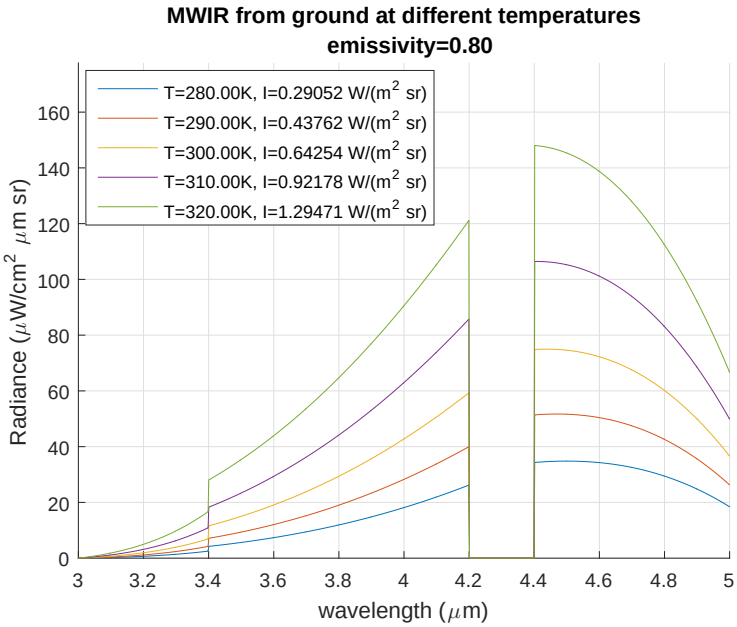

Figure 2.9: Ground emitted radiance after atmosphere

Focusing again on the MWIR window, the outgoing radiance, for a set of temperatures can be computed (Fig.2.9). The Thermal Emitted Radiance is only reduced by the atmospherical absorption during the path to space.

$$L_{out,emit}(\lambda) = L_{emit}(\lambda)\,\tau_a(\lambda) \tag{2.9}$$

As expected, increasing the temperature of the emitter, the *Planck's curve* peak

moves to the left at lower values of wavelength λ_{peak}, following the *Wien's displacement law* (Eq.2.10).

$$\lambda_{peak} = \frac{b}{T} \tag{2.10}$$

Where T is the emitter temperature and $b = 2.8977729\,10^{-3}\,mK$ is the *Wien's displacement constant*.
In other words, in view of the considered range of temperature, the thermal information collected observing the MWIR window will be higher as the temperature increases; in the LWIR instead is the opposite[3]. For that reason, a MWIR camera is subjected to lower environmental disturbes with respect to a LWIR camera[4].

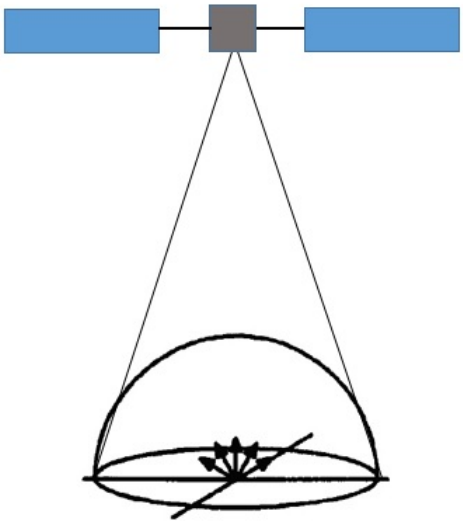

Figure 2.10: Schematization of a satellite looking at an extended Lambertian source

From the satellite point of view, the Earth must be modeled as an extended source. To simplify the problem, the ground can be considered as composed of flat square panels of dimension equal to the GSD[5], assumed to be *Lambertian sources* (Fig.2.10). A Lambertian source emittes radiance L homogeneously in all the directions, which means that the intensity of the radiance that reaches the satellite doesn't depend on the relative position of the observer[6].

2.1.4 Components Comparison

In order to estimate the power that will reach the satellite, it is necessary to integrate the Reflected and the Thermal Emitted Radiances along the MWIR window wavelengths.

$$I = \int_{\lambda_{min}}^{\lambda_{max}} L(\lambda)\, d\lambda \tag{2.11}$$

[3]This is one of the advantage in the use of MWIR
[4]Also the satellite itself is an emitter, but at low temperature
[5]The GSD is the projected dimension of a pixel on the ground, will be better introduced in 3.1
[6]In fact, this assumption is very close to the reality

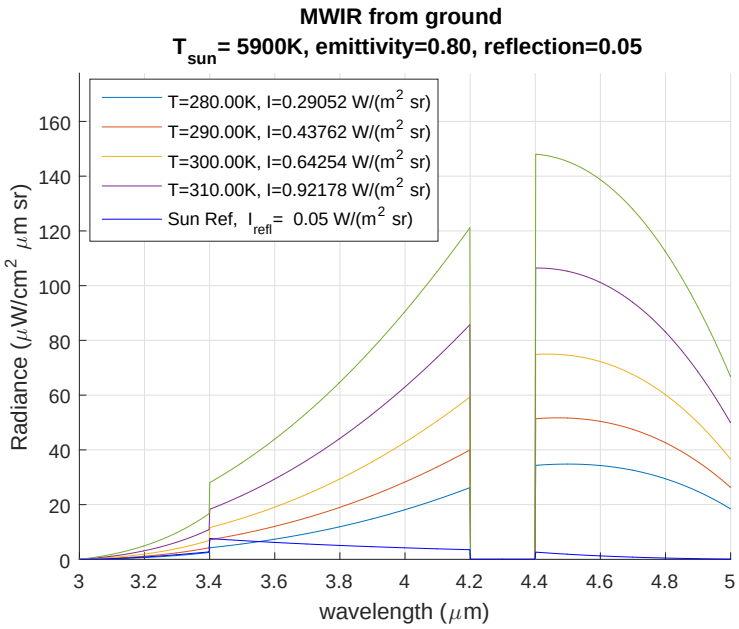

Figure 2.11: Sun Reflected - Thermal Emitted Radiance Comparison

As shown in the Fig.2.11 the Sun Reflected component is effectively comparable to the Thermal Emitted one and a way to remove or at least limit this component has to be found. For example, using a second camera which operate in the Visible it could be possible to compensate the Sun Reflected light. Another solution could be reduce the MWIR window moving the bottom limit closer to the upper one, where the Reflected Radiance is lower.
In any case, the Total Radiance that should reach the Spacecraft (I_{tot}) is given by the sum of the Sun Reflected and Thermal Emitted Radiances. In computing the performance quantities (e.g. SNR) the Sun Reflected Radiance has been assumed to be compensated and only the Thermal Emitted Radiance I_{emit} has been considered.

$$I_{tot} = I_{out,ref} + I_{emit} \tag{2.12}$$

2.2 Optics

The optical system collects the power which reaches the detector. In general, this is done by a set of lenses or mirrors, accurately designed and positioned (Fig.2.12).

When the optical system has to be chosen, some big differences between the two options must be taken into account:

- Mirrors are able to reflect a large portion of the spectrum, while lenses must be specialized for the observed bandwidth (e.g. glass is transparent to Visible light but not to Infrared).

- Lenses have aberrations problem: different wavelengths are refracted with different angles then, it is difficult to focus all the signal in a single point.

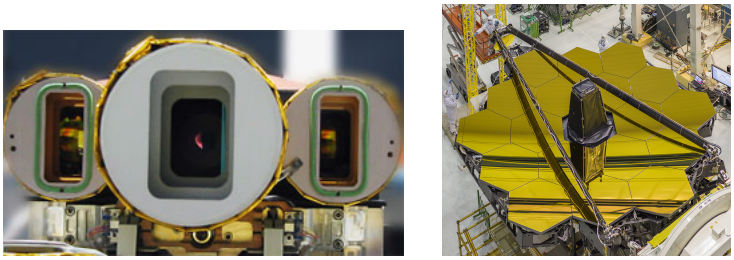

(a) (b)

Figure 2.12: (a) Lens based optics of TET-1 mission [5], (b) Mirrors based optics of Webb telescope. Image Credit: NASA

- It is easier to make a large mirror than a large lens. A mirror only requires fabrication on one side, while a lens requires both. Moreover, to obtain high-quality images, highly purified lenses are required, increasing the cost.

Basically, for big telescopes, a mirror based optics is certainly the best choice. Small satellites demonstrators usually look at only one or two bandwidths and, since the optics dimension must be contained, the trend is to use lenses[7].
Regardless of the collection principle choice, modern optical systems are composed of several lenses (or mirrors) positioned in order to make it more compact as possible.

For OUFTI-NEXT, a miniaturized hyperspectral imager for CubeSat, developed by *AMOS*, is the main candidate. The *AMOS*'s optics is designed with a Three Mirror Anistigmat (TMA) configuration (Fig.2.13) [14].

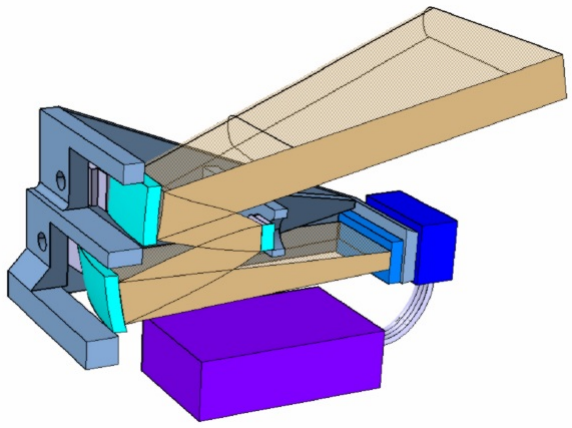

Figure 2.13: 3D section of the TMA telescope showing the mechanical structure, AMOS [14]

Since that work is part of a preliminary study it is not necessary to work on the physical system but it is enough to use an equivalent model to obtain significant results.

The TMA system has been modeled as a One Lens Optics (Fig.2.14), which trivially consider the optical system as made of only one lens, characterized by a

[7]Nevertheless, the use of the two systems on CubeSat is almost equivalent.

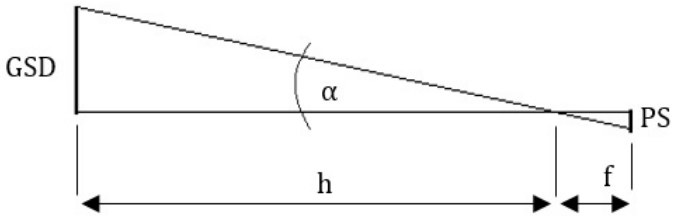

Figure 2.14: One Lens Model

diameter (D_p) and an equivalent focal distance (f). The behavior between these two quantities is in the f-number ($f/\#$), Eq.2.13.

$$f/\# = \frac{f}{D_p} \tag{2.13}$$

In that study, only the effect of Diffraction Limit will be taken into account, neglecting all the abrration effects.
The Diffraction Limit (D_l) represents a floor limit for the pixel dimension of the detector and is expressed by the *Abbe's law*.

$$D_l = 2.44\,\lambda\,f/\# \tag{2.14}$$

It is the smallest pixel dimension that allows to resolve (or distinguish) two consecutive images (Fig.2.15).

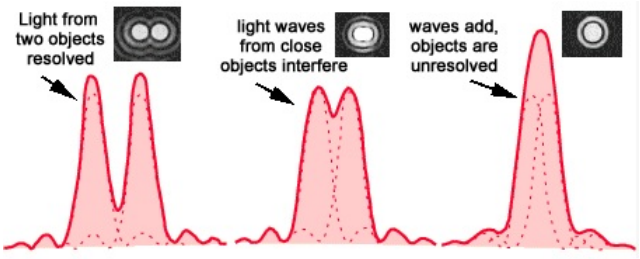

Figure 2.15: Diffraction limit effect [15]

This parameter is directly related to the optics $f/\#$ and the observed wavelength[8]. This formula put in evidence another advantage in observing MWIR instead of LWIR: since smaller wavelengths are observed, for the same optics it is possible to use smaller pixel and obtain lower GSD, or to use a smaller optics for the same pixel size.

2.3 Detector

The power collected by the optical system is directed to a detector. In this mission, a Charge Coupled Device (CCD) sensor is intended to be employed. This kind of sensor is able to collect photons into semiconductor material pixel that convert them

[8]Use for instance the central wavelength of the observed bandwidth.

into an electric signal. Then, an appropriate electronic device is able to read out the electric signal and then, a computer translates it into digital information. Several read out methods exist, basing on the array size and the kind of observation.

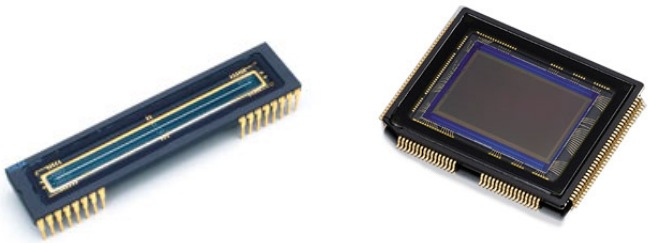

(a) **(b)**

Figure 2.16: (a) 1D & (b) 2D FPAs

CCD detectors generally consist of 1D/2D Focal Plane Array (FPA)[9], characterized by the pixel number (n rows x m columns), the pixel size (ps), and the pixel material (Fig.2.16).
What concern the pixel is strictly connected with the observed bandwidth. First of all, the material has to be sensible at the considered wavelengths (typically InSb in MWIR, Fig.2.17) and the choice of the size must be adapted to the Diffraction Limit. The FPA for this mission will be selected between what already available on the market.

Material	Bandgap (eV)	Center wavelength (µm)
GaP	2.4	0.52
GaAs	1.4	0.93
Si	1.12	1.1
InGaAs	0.73	1.7
Ge	0.68	1.82
InAs	0.28	3.5
InSb	0.16	5.5
HgCdTe	variable	variable
PbSnTe	variable	variable

Figure 2.17: Some typical sensor materials [10]

Detectors are electronic devices and, for this reason, electronic noises are always related to their use. In this preliminary study, only Read Out (RO) and Dark Current (DC) noises will be taken in to account.
The RO noise is due to the read out operation of the detector. The Dark Current instead, is due to the electrons thermal excitement and is the one that mainly affects the measures.

The DC noise is strictly related to the material properties (in particular the bandgap energy ΔE) and the operative temperature of the detector T_d. A way to

[9]FPA is an image sensing device consisting of an array (typically rectangular) of light-sensing pixels, positioned at the focal plane of a lens

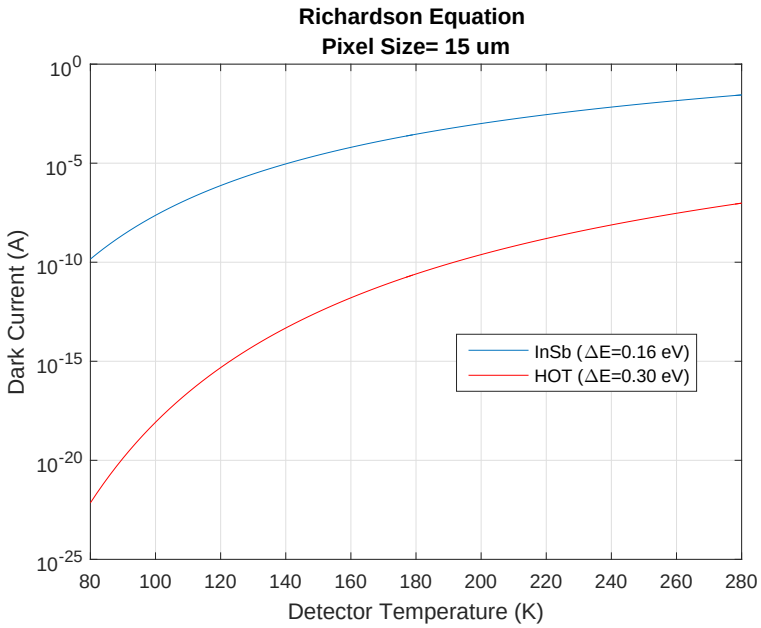

Figure 2.18: Examples of Richardson equation expressing Dark Current in function of Detector Temperature, for two different FPA's materials[10].

determine its value is given by the *Richardson's equation* [10]:

$$I_{DC} = C\, A_d\, T_d^2\, e^{\left(\frac{-\Delta E}{T_d}\right)} \tag{2.15}$$

Where k is the well known *Boltzman's constant*, $C = 1.2\,10^6\, A/(m^2\, K^2)$ is a constant parameter and $A_d = ps^2$ is the pixel area. This equation is not valid for all the materials, but it is a good approximation for the typical InSb FPA.
From Fig.2.18 it is clearly understandable the necessity of cool down that kind of detectors, in order to reduce the DC noise and be able to detect lower target temperatures with higher definition. Depending on the operative conditions, passive (using radiators) or active (e.g. Stirling cryo-systems) cooling system must be arranged[11].

This is one of the main issues in the use of IR detectors (especially in space applications), because the presence of the cooling system involves volume and weight growth, vibrations, and high alimentation power requirement. In fact, a continuous operational condition for a 3U CubeSat could be not sustainable, because the whole energy accumulated during light time would be barely enough for maintaine the cryogenic system. Hence, different scenarios have to be evaluated in the next design steps:

- increase the solar panels surface (passing to a bigger satellite or employing extendable panels);
- limit the use of cryogenic system at light time;
- increase the detector operational temperature (not recommended);
- improve passive cooling.

[10] HOT curve follows an adapted form of the law, provided by the producer.
[11] Uncooled bolometer sensors have been developed in the last years, but their use is reduced to operations that require high temperature targets and low definition images (such as fire detections).

Chapter 3

Parametric Studies

3.1 FOV and GSD

The main imaging parameters are determined by the combination of optics and detector characteristics, and by the orbit altitude (H) (Fig.3.1).

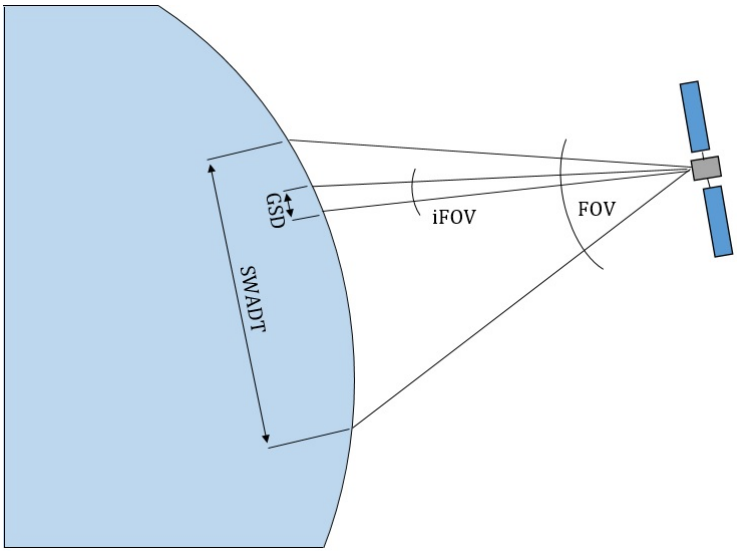

Figure 3.1: Schematization of main imaging parameters on one dimension

The Field Of View (FOV) is the angular aperture of the detector beam. A way to compute it is to pass through the Istantaneus Field Of View (iFOV). The iFOV corresponds to the field of view of the single pixel. With good approximation, it is possible to compute the iFOV basing on the one-lens geometry represented in Fig.2.14. Then, considering all the pixels to have the same iFOV, the FOV on the two dimensions are obtained summing the contribute of each pixel (or multiplying for the respective numbers of pixel).

$$iFOV = atan(\frac{ps}{f}) \tag{3.1}$$

$$FOV_1 = n\, iFOV \tag{3.2}$$

$$FOV_2 = m\, iFOV \tag{3.3}$$

The GSD, expressed in meter, is the linear dimension of a pixel projected on the ground. The next equation shows how to compute the GSD value at nadir, basing again on the one-lens geometry (Eq.3.4). In general, this value is not equal for all the pixel because the Earth has a curved surface. Hence, the GSD at nadir will be the smallest GSD value in the FOV. Assuming to have a narrow beam anyway, the GSD values do not substantially change and the curvature can be neglected.

$$GSD = \frac{ps}{f} H \tag{3.4}$$

One of the aims of this mission is to obtain the lowest GSD, in order to have the highest image resolution as possible. At this point, a parametric study is required, in order to understand how the GSD can be reduced. The following plots show the behavior between the GSD and the instruments and orbit characteristics.

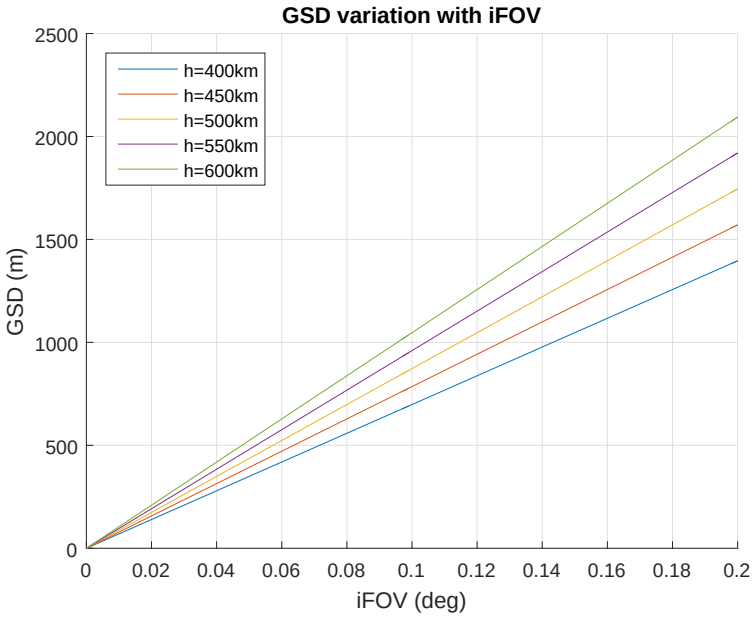

Figure 3.2: GSD variation with iFOV

The GSD is going to increase with the altitude and iFOV (Fig.3.2). An higher iFOV trivially means greater dimensions of the beam's cone (simple geometrical observation).
From Fig.3.3 and Fig.3.4 instead, it is possible to understand that, in order to achieve a low GSD, it is necessary to looking for a combination of a high focal distance optics and a small FPA pixel size.

Another useful parameter, that can be derived from GSD, is the Swadth. Assuming to have a small FOV (or narrow beam), the Swadth (SW) along the two dimensions can be computed [1],with good approximation, as

$$SW_1 = \frac{GSD\, n}{1000} \tag{3.5}$$

[1]It is more convenient to compute the Swadth in km. Hence, it is necessary to devide for a factor 1000 since the GSD is computed in meters.

$$SW_2 = \frac{GSD\, m}{1000} \tag{3.6}$$

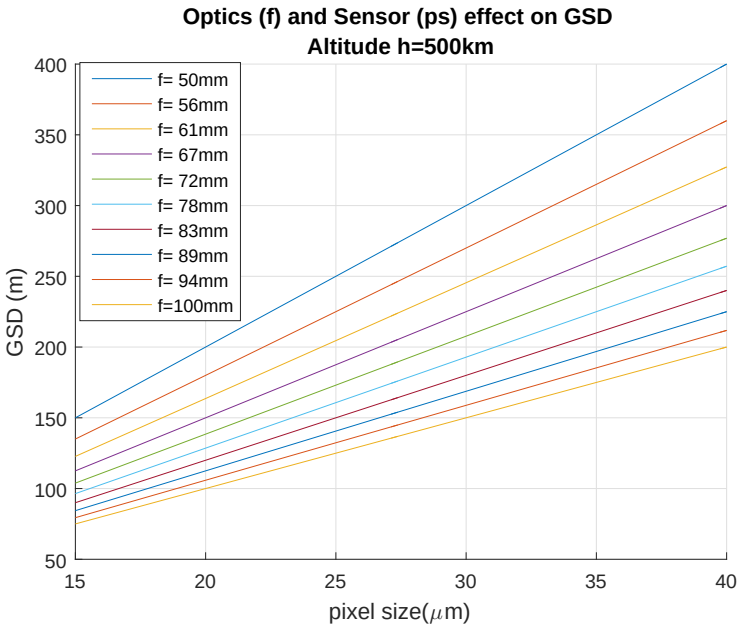

Figure 3.3: GSD for different optics/instrument couple

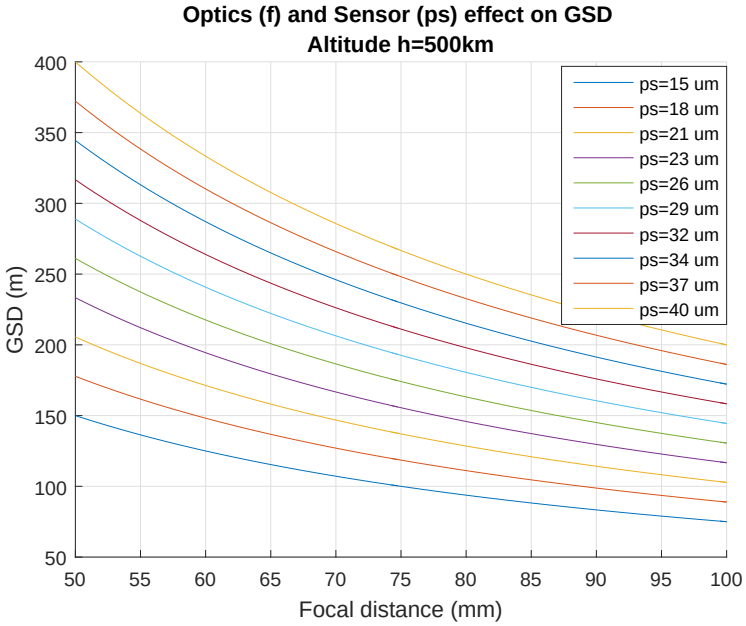

Figure 3.4: GSD for different optics/instrument couple

3.2 Curved Surface

As everybody (should) know, the Earth has a curved surface. Then, when a picture of the ground has taken from the space, the image will not be homogeneous in terms of resolution. In fact, moving from the center of the picture to the borders, the more external pixel visualize a larger surface than the one in the center. This effect can be large or contained, basing on the beam's cone aperture (wide or narrow). To evaluate if the Earth curvature is negligible, the surface corresponding to each pixel has been computed and then compared with the GSD at nadir.

To compute the GSD for each pixel, a geometrical approach is necessary (Fig.3.5). What is going to be explained is a 1D approach, which is equivalent along both the two dimensions.

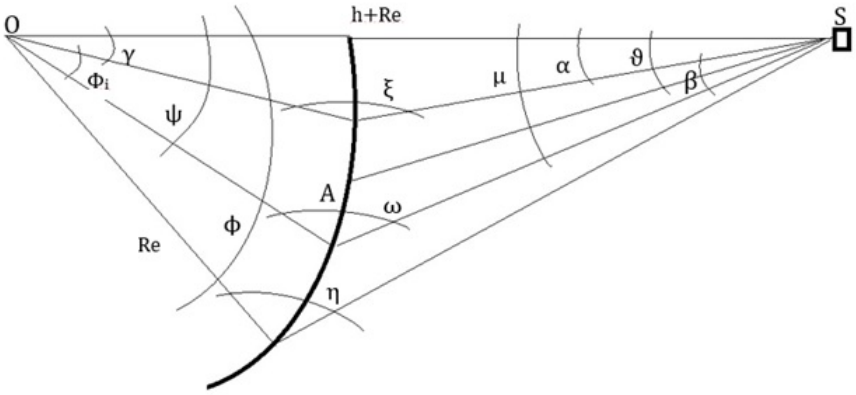

Figure 3.5: Earth scan geometrical representation

Assume that each pixel is watching at the Earth with the same iFOV which correspond to the angle β. If S is the Satellite position and O the Earth's center, each iFOV center line $\overline{SA}$ is rotated by an angle θ from the FOV centerline $\overline{SO}$ in order that the sum of the iFOVs corresponds to the total FOV.
By using sine law, it is possible to compute ω and as consequence ψ.

$$\omega = \pi - \arcsin\left(\frac{H + R_e}{\sin\theta + \frac{\beta}{2}}\right) \tag{3.7}$$

$$\psi = \pi - \omega - \left(\theta + \frac{\beta}{2}\right) \tag{3.8}$$

Where H is the orbit altitude and R_e the Earth radius. Then, define the angle α as:

$$\alpha = \begin{cases} \dfrac{\beta}{2} & \text{if } \theta = 0 \\ \theta - \dfrac{\beta}{2} & \text{if } \theta \neq 0 \end{cases} \tag{3.9}$$

And by using again the sine law, compute the angle ξ and γ.

$$\xi = pi - \arcsin\left(\frac{H + R_e}{\sin\alpha}\right) \tag{3.10}$$

$$\gamma = \pi - \xi - \alpha \tag{3.11}$$

The angle ϕ_i corresponds to the scanned angle with respect to the Earth's center. Hence, knowing this angle it is enough to multiply it for the Earth radius to obtain the scanned arc length for each pixel.

$$\phi_i = \psi - \gamma \tag{3.12}$$

$$GSD_i = \phi\, R_e \tag{3.13}$$

Summing all the GSD_i the real Swadth can be obtained.
At this point it is possible to define a GSD rate with respect to the nadir GSD, in order to have a value that allows evaluating if the Earth curvature can be neglected or not.

$$GSD_{gain} = \frac{GSD_i}{GSD_{nadir}} \tag{3.14}$$

Moreover, it is also possible to compute the scanned surface for each pixel. Computing with the same procedure the scanned angle ϕ_i and χ_i on the two dimensions, the scanned surface S_i is the result of the surface integral centered on the iFOV centerline. Obviously, the total scanned surface S_{tot} is given by the sum of all the contributes.

$$S_i = R_e^2\, \chi_i \left[\cos\Big(\frac{\pi}{2} - \frac{\phi_i}{2}\Big) - \cos\Big(\frac{\pi}{2} - \frac{\phi_i}{2}\Big)\right] \tag{3.15}$$

$$S_{tot} = \sum S_i \tag{3.16}$$

3.3 Signal to Noise Ratio

With the GSD, the second most important parameter is the SNR. Its value gives a direct information on the real possibility to obtain useful thermal information from the ground. Different techniques to evaluate the SNR exist, but since this work is going to be a feasibility study it is enough to predict the correct order of magnitude, using the simplest formulas as possible.

3.3.1 Linear Scan

The simplest way to scan the ground is to use a 1D CCD sensor and make it scan the ground along the direction normal to the spacecraft velocity. The principle is the same of an office scanner, the FPA collects photons for a maximum exposure

time equal to the time required by the spacecraft to travel a distance equal to the GSD. Then, the electronics read out the electrical signal from the pixel. After that, the pixel line starts collecting photons coming from the immediately next portion of ground. In that way, the image along the flight direction is automatically built by the satellite's movement (Fig.3.6).

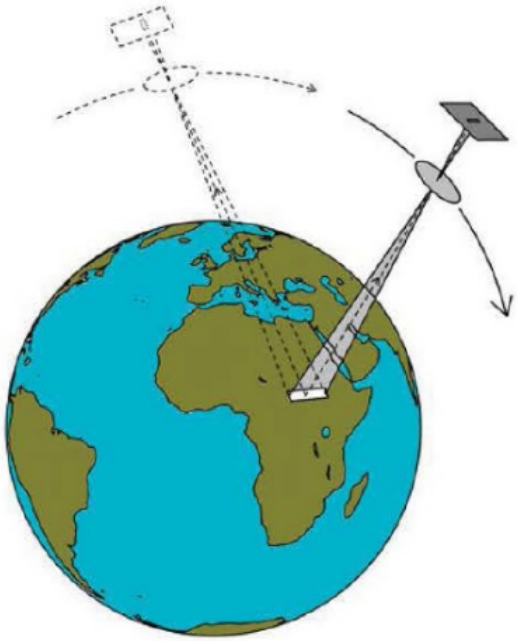

Figure 3.6: Linear Scan [16]

The maximum exposure time for the pixel row, for each portion of ground, is dictated both by the GSD dimension and the spacecraft velocity with respect to the ground. Assume that the spacecraft is traveling on a circular orbit, knowing the orbit altitude the Orbit Period (T_o) can be computed with the *Third Keplerian's Law* (Eq.3.17).

$$T_o = 2\,\pi\,\sqrt{\frac{a^3}{\mu_e}} \tag{3.17}$$

Where μ_e=398600 km^3/s^2 is the Earth Gravitational Parameter and a is the semi-major axis of the orbit which for a circular orbit is equal to the orbit radius. Hence, a is the sum of the Earth Radius (R_e=6371km) and the Orbit Altitude.
It is then possible to compute the Spacecraft Velocity with respect to ground V_{sat} (km/s).

$$V_{sat} = \frac{2\,\pi}{T_o}\,R_e \tag{3.18}$$

The orbital angular velocity $n = 2\,pi/T_o$ must be divided for the Earth radius because the velocity of interest is referred to the ground[2].
This result is still not accurate because the Earth angular velocity ($\omega_E = 7.29\,10^{-5}\,rad/s$) has not been taken into account but, considering that the orbit angular velocity for an 800km height orbit is $\omega_{sat} = 1\,10^{-3}\,rad/s$, it is possible to neglect it. Again,

[2]Dividing by a the spacecraft velocity in the space would be obtained.

reaching the correct order of magnitude is sufficient for the purpose.

Assuming that the computed V_{sat} will be constant in time, it is immediately possible to compute the Integration Time T_i[3].

$$T_i = \frac{GSD}{1000\, V_{sat}} \tag{3.19}$$

3.3.2 Signal

Starting from the radiance that reaches the pupil, it is possible to compute the collected Signal. The emitted power, corresponds to the flux of photons that reaches the sensor. Consecutively, it is possible to recover the number of electrons read-out by the electronics. To do that it is necessary to start evaluating the irradiated power that reaches a pixel.

Power Collected by Pixel

First of all, in order to sum up the contributes of all the observed wavelengths, the radiance at the pupil has to be integrated into the observed bandwidth[4].

$$I_{pupil} = \int_{\lambda_{min}}^{\lambda_{max}} L_{pupil}(\lambda)\, d\lambda \tag{3.20}$$

Then, looking at the definition of radiance, to obtain the power it is necessary to multiply I_{pupil} for the emitter surface $A_s = GSD^2$ and for the solid angle Ω_{OS}[5]. These two quantities can be computed from the GSD and knowing the orbit altitude and the pupil diameter. Hence, they change for each different fly condition. As consequence, they should be recomputed at each change, and the results are affected by numerical approximations.

$$\Omega_{OS} = \frac{A_p}{H^2} = \frac{\pi\, D^2}{4\, H^2} \tag{3.21}$$

Where A_p is the Pupil Area.
The etendue T is defined as the product of a surface area and the solid angle exiting the source that reaches the observer.

$$T = A\,\Omega \tag{3.22}$$

Thanks to the *Etendue invariance* (Fig.3.7) it is possible to use different couples of surface and solid angle [10].

$$T = A_s\,\Omega_{OS} = A_o\,\Omega_{SO} = A_o\,\Omega_{DO} = A_d\,\Omega_{OD} \tag{3.23}$$

In particular, the couple $T = A_d\,\Omega_{OD}$ is the most accurate and immediate. The detector Area A_d correspond to the Pixel Area ($A_d = ps^2$) and the Optics Solid

[3]Since the GSD is expressed in meter and the velocity in km/s, it is necessary to divide by a factor 1000.
[4]It depends on the FPA cutoff.
[5]Ω_{OS} is the solid angle exiting the source that reaches the pupil.

Angle Ω_{OD} is related only with the $f/\#$, which has a fixed value.

$$\Omega_{OD} = \frac{\pi}{4\, f/\#^2} \tag{3.24}$$

Moreover, the *Etendue Invariance* lead to the fact that, fixed the optics and the sensor, T will be a constant value, independently by the orbit altitude.

After computed a precise etendue value, it is possible to compute an accurate result for the Power (P).

$$P = I_{pupil}\, A_d\, \Omega_{OD}\, \tau \tag{3.25}$$

Where τ is the optics transmission coefficient.

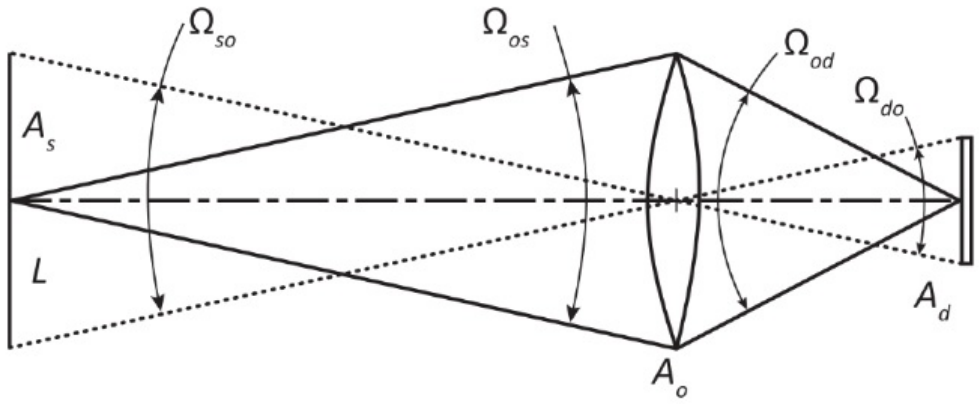

Figure 3.7: Etendue Invariance [10]

Number of Electrons

Knowing the Power, it is possible to express it as the photons flux that reaches the pixel F (e^-/s).

$$F = P\, \frac{\lambda}{h\, c}\, q_{eff} \tag{3.26}$$

Where h and c are again the *Planck's constant* and the *Speed of light*, and q_{eff} is the detector quantum efficiency[6].

Finally, the number of electrons that reach the pixel, is trivially obtained multiplying F to the Integration Time.

$$S = F\, T_i\, TF \tag{3.27}$$

Where TF is the transmission coefficient of the linear filter.
The Signal is directly dependent by the Integration Time. It is possible to plot some curves of the Signal collected for different source temperatures for a range of orbit altitudes (Fig.3.8). From this plots, it is clear that, despite H affects several terms, the global effect in the Signal is close to a direct proportionality. In fact, the variation on the GSD and the solid angle can not be felt because their product is constant. Hence, the only quantity which changes is the Integration Time which increases with H.

[6]Represent the efficiency of the detector in convert photons in electrons.

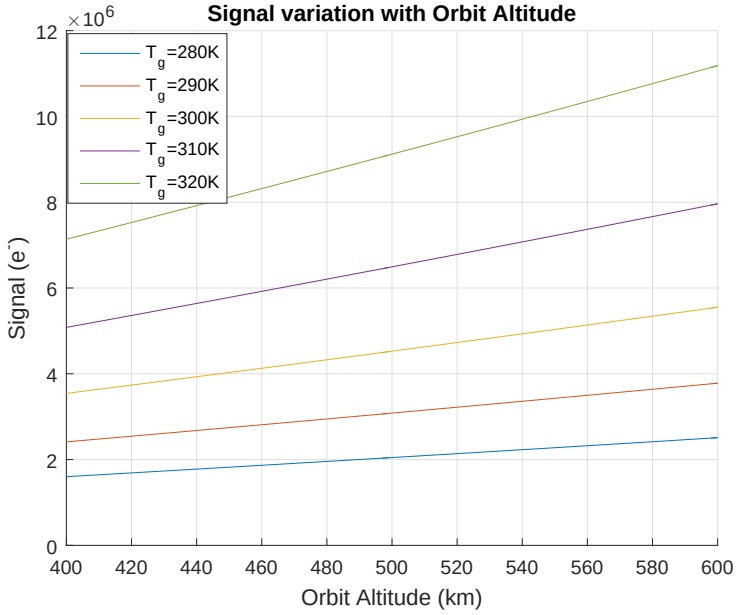

Figure 3.8: Signal variation with orbit altitude for different ground temperatures

3.3.3 Noise

Noises due to the electronics have been already introduced (2.3). To compute the SNR, it is necessary to express also the noises in terms of number of electrons. Usually, the Read-Out Noise is already present in the detector datasheet with the required unit of measure, while the Dark Current has to be converted from an electric current value (A). The electric current is equivalent to a charge flux (C/s). Hence, it is possible to convert the charge value in number of electrons, knowing that the electron's charge is $Q_e = 1.60217662\,10^{-19}\,C$ and multiplying for the Integration Time.

$$N_{DC} = \frac{I_{DC}}{Q_e}\,T_i \tag{3.28}$$

Another noise source is the Signal itself. In particular, the Signal Noise (N_s) is defined as

$$N_S = \sqrt{S} \tag{3.29}$$

Finally, the global effect of all the contributes can be extracted computing the square root of the sum of the square of all of them.

$$N = \sqrt{N_S^2 + N_{DC}^2 + N_{RO}^2} \tag{3.30}$$

Actually, an accurate noise determination is not so trivial and would require a large effort but again, it is not necessary at this stage.

3.4 SNR Parametric Study

The SNR is for definition the rate between the acquired Signal and the Noise.

$$SNR = \frac{S}{N} \tag{3.31}$$

The result of this rate depends on several factors, which have been already presented during Signal and Noise evaluations (3.3.2 and 3.3.3). In fact, the majority of the factors that affect the SNR are varying the Integration Time, that consequently becomes the main reason of SNR variations. The Signal is directly dependent by the Integration Time while the noise varies with its square root (only DC noise depends on it). Hence, the SNR varies by the square root of T_i.

3.4.1 Optics effect on SNR

With the One Lens model, the optical system can be characterized by the focal distance f and the $f/\#$. In Fig.3.9 the variation of the SNR with the $f/\#$, for different values of f is shown.

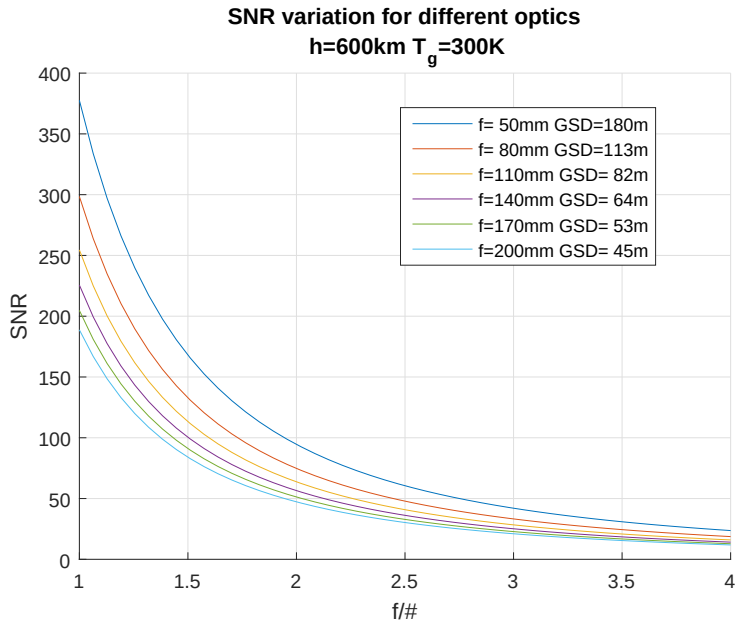

Figure 3.9: SNR for different optical quantities combination

Change the $f/\#$ means to change the Solid Angle which determines the Signal quantity. Increasing the $f/\#$ the Signal and as consequence, the SNR decreases. In the other hand, from the definition of the $f/\#$ as it increases the pupil diameter decreases (Eq.2.13)[7]. Increase the focal distance instead means decrease the GSD. Despite one of the targets of the project is obtain a small value for GSD, smaller GSD means less Integration Time and then a decrease of SNR (as the square root of T_i). Hence, a good compromise in the choiche of the $f/\#$ has to be found.

[7]For equal focal distance.

3.4.2 Detector effect on SNR

The detector model is defined by the pixel size, by the Read-Out Noise, and by the DC generation (Detector Temperature). The effect of these quantities on the SNR is shown in Fig.3.10

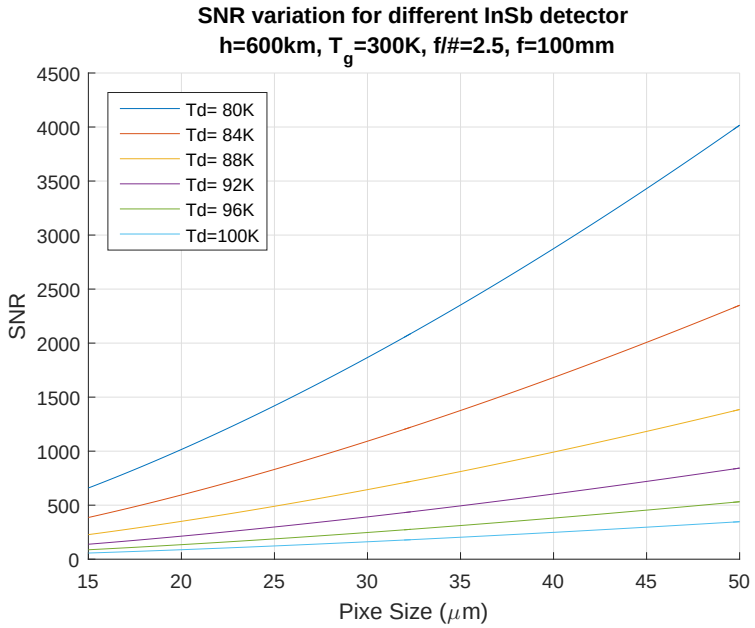

Figure 3.10: SNR variation for different InSb detectors

Higher is the Detector Temperature higher is the DC Noise and, as consequence, lower the SNR.
The pixel size instead affects both the Dark Current Noise and the Signal. Bigger pixel means bigger GSD and higher Integration Time, but also higher DC Noise. The global effect is that the SNR increases. But again, the SNR and GSD follow opposite trends and also a compromise for the pixel size should be found. Nevertheless, in this work, the smallest possible pixel size will be chosen.

3.4.3 Altitude and Ground Temperature effect on SNR

The last factors to be considered are the Ground Temperature and the Orbit Altitude (Fig.3.11). The Ground Temperature determines the amount of emitted power. Referring to the *Planck's curve*, for the range of temperature of interest[8], higher is the temperature higher is the emission in the MWIR.
The orbit altitude instead acts on the Integration Time. Higher is the orbit, lower is the satellite velocity and larger is the GSD. Both those change, have as consequence an increase of Integration Time, which means an increase of SNR. Again, a good compromise should be found, but the orbit altitude is first dictated by the launch availability[9].

[8] Temperatures lower than 345K.
[9] CubeSats are launched as secondary payloads or deployed from the International Space Station. Then, the orbit can not be choosen at priori.

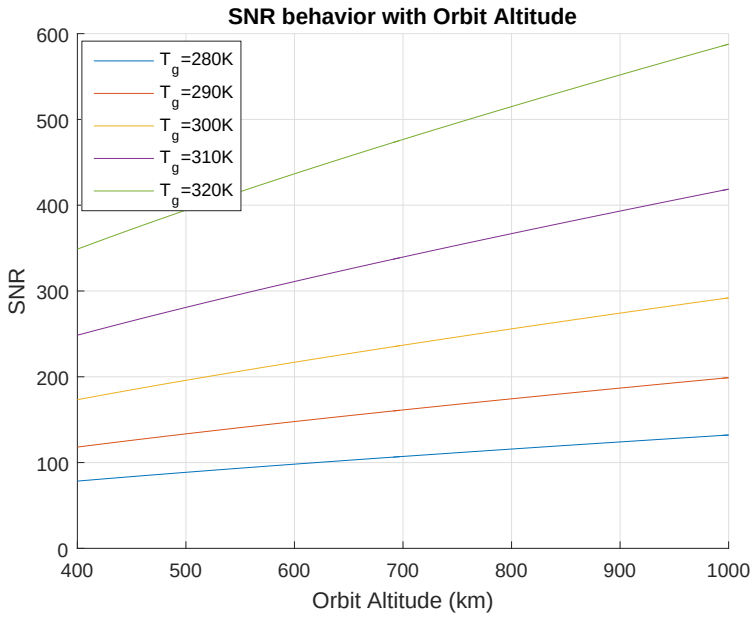

Figure 3.11: Effect of the Orbit Altitude on the SNR for different Ground Temperatures

Table 3.1: GSD and SNR trends

	GSD	SNR
iFOV	↑	↑
H	↑	↑
f	↓	↓
ps	↑	↑
$f/\#$	↓	↓
T_d	//	↓
T_g	//	↑

In Tab.5.1 are summarized the effect of the studied parameters increment, on GSD and SNR[10].

3.5 SNR improvement

Until now the Single Line scan method has been considered in computations. However, the Integration Time (and hence the SNR) can be increased modifying the scan method. Employing a 2D FPA sensor instead of a single line detector, different solutions can be adopted.

A first option is given by the Time Delay Integration (TDI) scan. TDI technology

[10]The variations in GSD and SNR must be considered for parameters increment.

is used for applications with relatively fast movement between the camera and the object being captured. A 2D FPA is employed, e.g. 128x256. The image is captured only on one dimension then, the 256 columns composed by 128 pixel will perform a linear scan on the same ground portion.

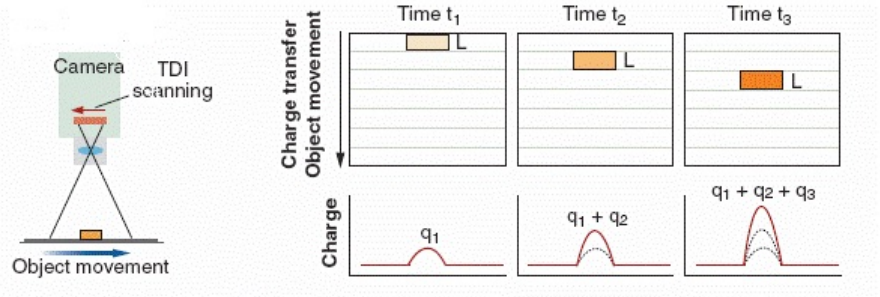

Figure 3.12: TDI scan representation [17]

In the TDI mode, the same object is imaged multiple times (Fig.3.12). As the image moves from one row of pixels to the next, the generated charge moves along with it, noiselessly integrating with the previously generated charge. This provides a higher sensitivity at low light levels than can be achieved with a traditional line scan camera.
That lead to directly increment the integration time, and then the collected power, by the number of columns m. As already seen the SNR depends on the square root of the Integration Time, hence the SNR is increased by a factor equal to the square root of the m (Fig.3.13).

A second way to improve the SNR can be the use of the Attitude and Orbit Control System (AOCS). Instead of scanning the ground, is it possible to take a

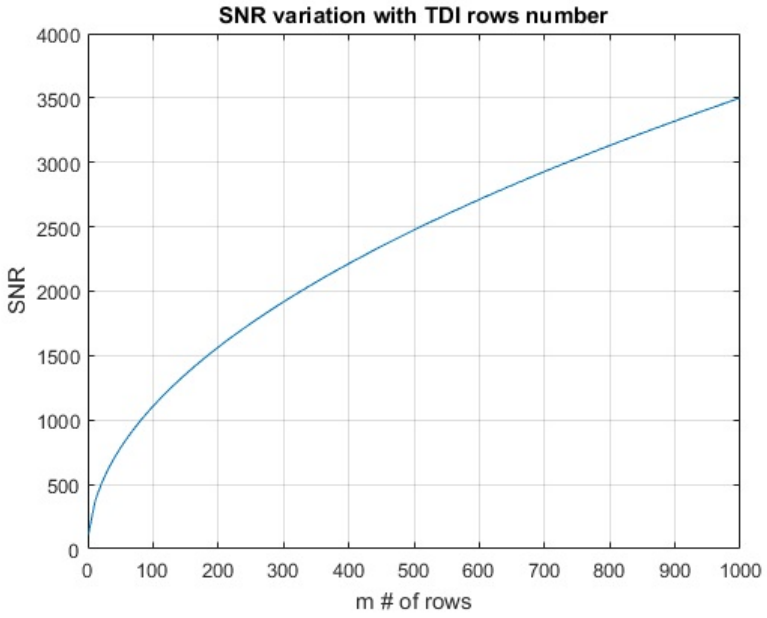

Figure 3.13: SNR improvement with TDI scan

shot of the desired area (Area Scanning), but the integration time is still related to the GSD travel time. The idea is to employ the attitude control system in order to track the on ground target, increasing the Integration Time (Fig.3.14).

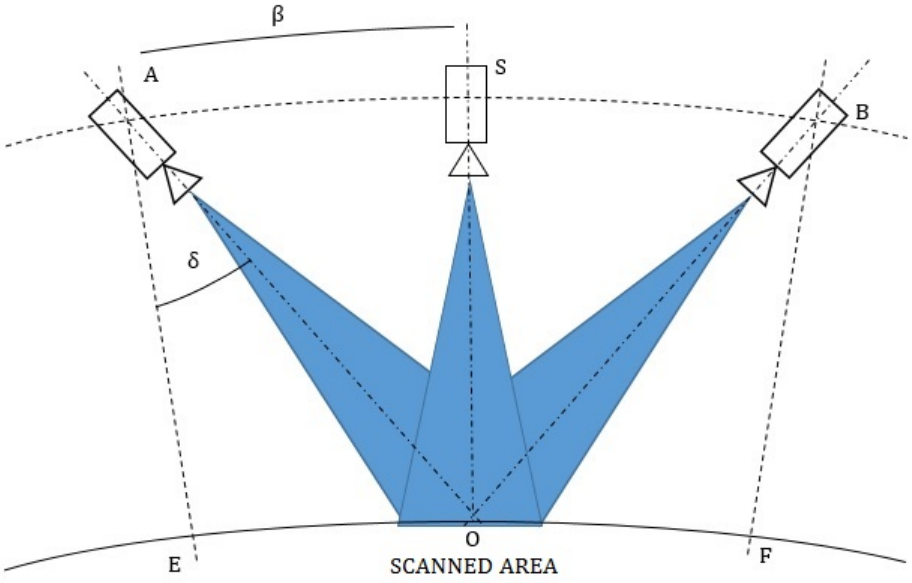

Figure 3.14: Scheme of SNR improvement with AOCS scan

Normally, while scanning the ground, the Spacecraft is performing an Earth pointing. In other words, it is rotating on an axis normal to the orbital plane at an angular velocity (Ω_{sat}) equal to the orbital one (n), in order to always pointing at the center of the planet.

$$n = \frac{2\,\pi}{T_o} \tag{3.32}$$

To increase the exposure time, it is necessary to observe the target also before and after the nadir position. This prolungated observation can be obtained tilting the satellite and performing a Target pointing where $\Omega_{sat} \neq n$. An example of the procedure is here reported:

1. Early rotate the Spacecraft to the angle that allows to move up the target pointing. How much before depends on the desired exposure time.

2. Start following the target with an $\Omega_{sat} \neq n$.

3. Proceed with Target pointing up to reach the desired Integration Time. The final Spacecraft attitude should be specular to the starting one.

Referring to the Fig.3.14, defining G as a Gain factor for the Integration Time with respect to the Linear Scan, the spacecraft must start the Target pointing (2) with an anticipation equal to T_d.

$$T_d = \frac{T_i}{2}\,G \tag{3.33}$$

This anticipation in time corresponds to an advance in angular position on the orbit (β) at wich the observation begin[11].

$$\beta = T_d\, n \tag{3.34}$$

Then, the length of the arch corresponding to the angle β on the Earth surface (EO) is given by the Earth curvature assumed to be spherical.

$$EO = \beta\, Re \tag{3.35}$$

The segment $\overline{EA}$ it's equal to the orbit altitude H. Assuming to looking to the ground with a narrow beam and that β is a small angle, it is possible to approximate the arch EO with a segment ($\overline{EO}$). Consequently an approximation for the initial tilt angle of the Spacecraft (δ) and the Target pointing angular velocity can be found.

$$\delta \approx atan\left(\frac{\overline{EO}}{\overline{EA}}\right) \tag{3.36}$$

$$\Omega_{sat} = \frac{\delta}{T_d} \tag{3.37}$$

Compared with the TDI this method requires more efforts, because it implies the design of an appropriate attitude control. Moreover, it does not allow to have a continuous scan. The target position must be well known and it is necessary to synchronize the pointing. In the other hand, this method gives more flexibility. In fact, the TDI SNR improvement is fixed with the FPA dimensions while the use of an Attitude Control is limited by the actuators performances, making it much flexible.

Both the possible scenarios are limited by the reachable attitude stability during the Integration Time: the spacecraft will never be completely at rest, continuously oscillating around its equilibrium point. However, it is enough to do not deviate from the GSD during the photon collection (e.g. move for less than 0.5 arcminutes during 2s of exposure time).
These two methods have been presented because they are the most simple and adaptable on small CubeSats. Here is a summary of the two systems characteristics:

- TDI
  - requires only electronic effort
  - SNR improves with square root of columns number (pay attention: too many columns can saturate the pixels at too low target temperature)
  - the scanning is still continuous along the orbit, no need to synchronize the scan with the target position
- AOCS
  - control law has to be designed

[11] It depends on the orbital angular velocity and then the orbit altitude.

- requires appropriate actuators
- the scanning is discretized along the orbit, the target position must be well known and the AOCS-SCAN has to be synchronized with it (the observation window opens before and closes after the regular time)
- the gain in exposure time is not fixed

Table 3.2: Example of SNR evaluation for different scan methods using a 640x512 CCD detector (640 spatial dimension in linear based scans).

Ground Temperature	SNR (Linear Scan) $T_i = 0.0302s$	SNR (TDI) $T_i = 15.46s$	SNR (AOCS) $T_i = 0.1510s$
290.98K	1367.6	30944.6	3285.7
292.24K	1413.4	31980.5	3387.3
293.49K	1459.9	33033.5	3490.4
294.75K	1507.2	34103.6	3595.1
296.01K	1555.2	35190.7	3701.3
297.26K	1604.0	36294.8	3809.1
298.52K	1653.6	37415.8	3918.4
299.77K	1703.8	38553.5	4029.2

3.6 Thermal Resolution

After the signal power has been collected and converted into electrons, it has to be associated with a value of the ground temperature. The sensitivity of the measures depends on the SNR and the instrument's digital resolution. In other words, the uncertainties of the measures are due to the relative effect of the noise on the acquired signal. In this chapter an attempt to roughly evaluate the Thermal Resolution[12] of the caugth pictures is going to be described.

3.6.1 Signal to Temperature Behavior

To obtain a value of the Ground Temperature from the acquired Signal, it is necessary to invert the *Planck's law*. An analytical expression, in this case, is complicated and could require too many approximations in going back from a power to a radiance. Then, numerically build a polynomial expression of the curve become easier (Fig.3.15).

The instrument is ideally going to read Signal from the zero value to a maximum (depending on the sensor). In this problem, the value of zero signal is associated with several temperatures. To obtain a more accurate polynomial it is then useful

[12]The Thermal Resolution must be interpreted as the minimum detectable difference of temperature.

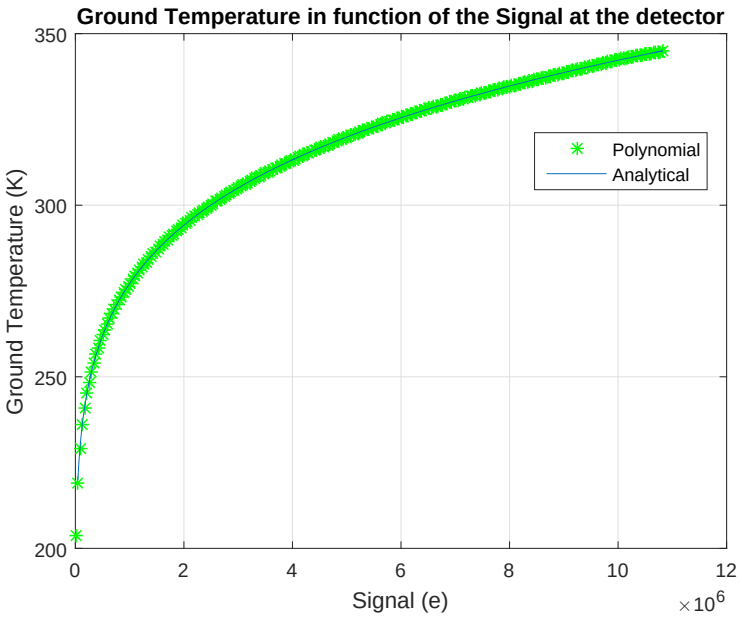

Figure 3.15: Analitical and Polynomial curves of Ground Temperature in function of the incoming Signal

to select a smart range of temperatures. For instance, set as minimum value the first temperature which give a close enough to zero signal (e.g 200K) and as maximum value a temperature not too far from what is expected to measure (e.g. 340 K) .

At this point, the signal must be converted to digital form. Hence, the incoming signal scale must be quantized.
Knowing the digital resolution of the instrument n_{bit}, the Signal scale can be divided in $M = 2^{n_{bit}}$ intervals. Each intervals extensions is equal to the signal step q.

$$q = \frac{S_{max} - S_{min}}{M} \tag{3.38}$$

The Fig.3.16 shows the application of the quantization to the polynomial behavior. Observe that, since the quantization is applied to a curve, the temperature variation between two signal steps will not be a constant value.

3.6.2 Detectable Temperature Sensitivity

After discretizing the signal to temperature curve, the quantization error has to be introduced. The curve has become a stair and then the temperature measures are also separated by steps[13] (T_{step}).
At this point, the effect of the noise has to be introduced. The noise is a random quantity and what is known is the maximum value that it can assume. That value can be found passing through the SNR:

- compute the value of the measurable Temperatures T_{bit} corresponding to the discretized Signal values S_{bit}

[13]The amplitude of the stpes is variable because of the non-linear nature of the behavior.

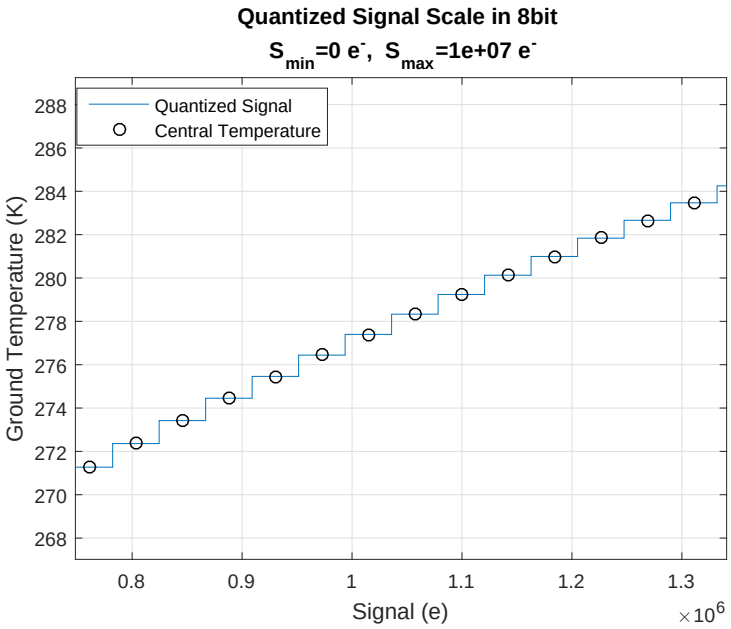

Figure 3.16: Quantized Signal Scale

- compute the corresponding SNR for all the T_{bit}
- recover the noise values N_{bit} using the SNR definition

Then, the noise for each signal value can be compared with the Signal Step q.

$$N_{q\%} = \frac{N_{bit}}{q}\,100 \tag{3.39}$$

The parameter $N_{q\%}$ expresses the effect of the noise on the quantized curve. In other words, it is an index of the measurement stability. In fact, higher is the noise, larger are the oscillations of the detected signal. Then, the measured temperature can randomly move between two or more steps.
Finally, The Thermal Resolution ΔT, which actually represents the sensitivity of the measure, has been defined as follow.

$$\Delta T = \begin{cases} 2\,T_{step} & \text{if } N_{q\%} \leq 50\% \\ (ceil(0.01\,N_{q\%}) + 1)\,T_{step} & \text{if } N_{q\%} > 50\% \end{cases} \tag{3.40}$$

In the first case ($N_{q\%} \leq 50\%$) the main error is due to the discretization of the scale. Then, the maximum oscillation of the measure will be between two consecutive steps (Fig.3.17).

In the second case ($N_{q\%} > 50\%$) the noise oscillations easily exceed the Signal Step q. As consequence, the amount of get involved T_{step} are more than two (Fig.3.18).

It is preferred to always be in the first case in order to make the most use of the digital resolution[14].

[14] If necessary, decrease digital resolution.

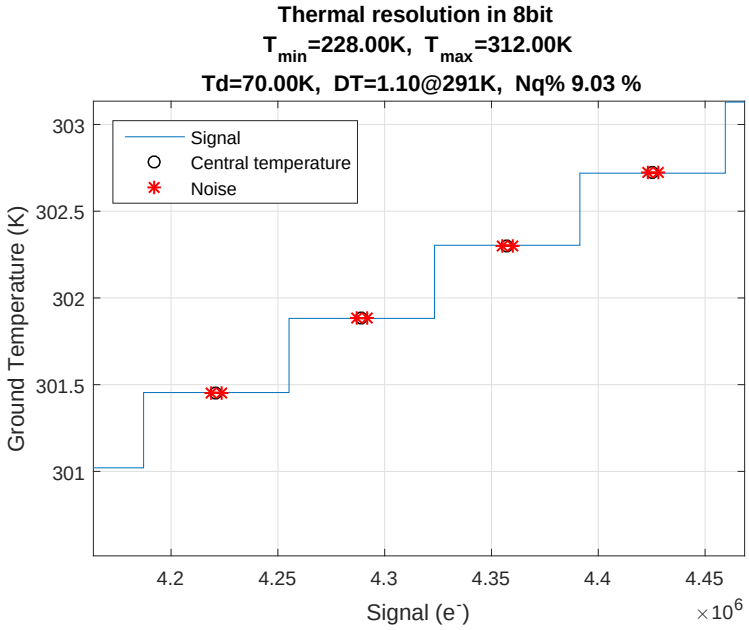

Figure 3.17: Thermal Resolution for $N_{q\%} \leq 50\%$

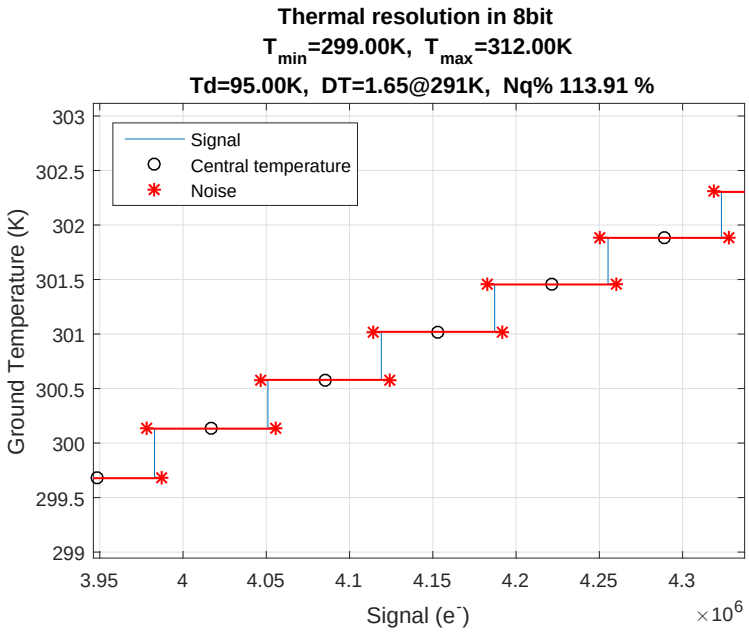

Figure 3.18: Thermal Resolution for $N_{q\%} > 50\%$

At this point, the minimum and the maximum detectable temperature can be defined and computed.
The minimum detectable temperature T_{min} is the one at which correspond the minimum SNR requested to have a good measure[15]. The maximum detectable temperature T_{max} instead is given by the Well Capacity (S_{max}). The Well Capacity represents the maximum number of electrons that can be collected by the pixel[16].

[15] SNR=100 has been arbitrarly chosen.
[16] A margin of 10% has been arbitrarly left, so consider 0.9 time the datasheet value.

Observe that, increase the SNR means to increase the thermal sensitivity (lower ΔT) and T_{min}. However, at the same time T_{max} decreases. Hence, due to the nonlinear nature of the problem, the thermal scale tends to shrink.

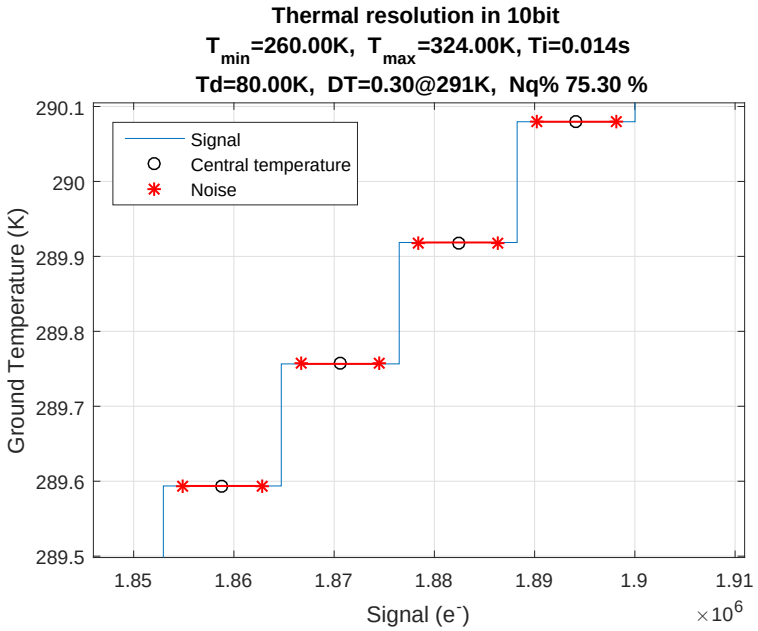

Figure 3.19: Thermal Resolution with linear scan, 640x1 CCD

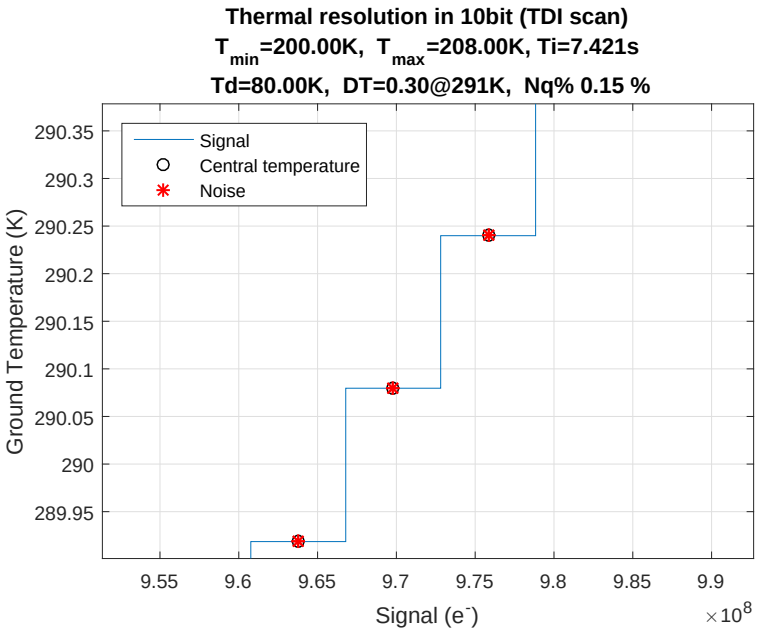

Figure 3.20: Thermal Resolution with TDI scan, 640x512 CCD

Another equilibrium has to be found. To improve the thermal sensitivity, it is possible to increase the digital resolution, reducing the thermal step due to quantization. But, at the same time, the noise effect become larger on the measure because q has been reduced. Hence, a higher SNR is required.

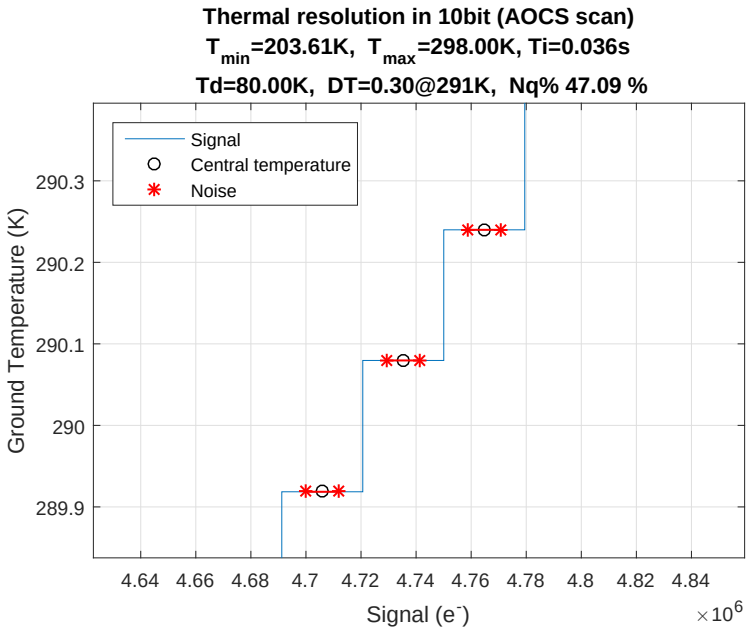

Figure 3.21: Thermal Resolution with AOCS scan, 640x512 CCD

The employment of SNR improvement methods (TDI or AOCS) can help in increase the thermal sensitivity, allowing the use of higher digital resolutions. In the following example, a 10bit quantization has been performed for a relatively high-temperature detector ($T_d = 80K$). For a simple linear scan, the measured noise is the major reason of uncertainties, that means that the high quantization resolution can not be actually used (Fig.3.19).

Upgrading to a TDI scan the SNR is higher and become possible to make the best use of the small step quantization (Fig.3.20). Unfortunately, the higher SNR is given by the acquisition of a higher Signal and not by a detector enhancement. As consequence, the pixel saturation occurs at lower temperatures, narrowing the detectable temperatures range. The TDI scan is determined by the array dimensions and then, the gain in SNR is not adjustable.

Incrementing the SNR by the use of AOCS allows to the possibility of choose the SNR Gain[17] in order to find (if necessary) a good half-way between Linear and TDI scans (Fig.3.21).

These results remark the necessity of use low noise detectors as base for SNR increment; otherwise, the attempts to increase the Signal could become unusable.

[17] Always being in the feasibility limits

Chapter 4

Simulations

All the models introduced in the previous chapters, have not been imaged only for performing the parametric studies, but also to evaluate the instrument characteristics necessary to accomplish the mission's goal. Hence, a software that combines all the ground, optics, detector and orbital parameters has been developed to simulate the observation performances.

4.1 Developed Software

In Tab.7.1 the input/output variables of the script are listed. The input variables will be set in order to have realistic values, usually extracted from supplier's datasheet or based on user's reasonings.
In Fig.4.1 the blocks scheme representing the software structure for Linear and TDI scan simulation is shown and the same for AOCS scan in Fig.4.2.

Only a few constraints can be applied to the input variables:

- The pupil must be contained in 10cm then, only values lower than 6cm for its diameter will be accepted.

- Concerning the detector, the selection has been restricted looking for the lowest possible pixel size. On the market are present several FPA sizes employing 15 or 20 μm. Only these two values will be taken into account. The other data are extracted by datasheet of detectors which respect this specific.

- It is not possible to predict the exact orbit. The satellite will be put in a LEO but the exact altitude will depend on the launch availability. Then, orbits between 400km and 800km will be studied, or at least the results' excursion on these two extremes.

This software can be used for two different purposes, taking one as consequence of the other:

1. Required hardware characteristics prediction.

2. Performance evaluation of the chosen instruments.

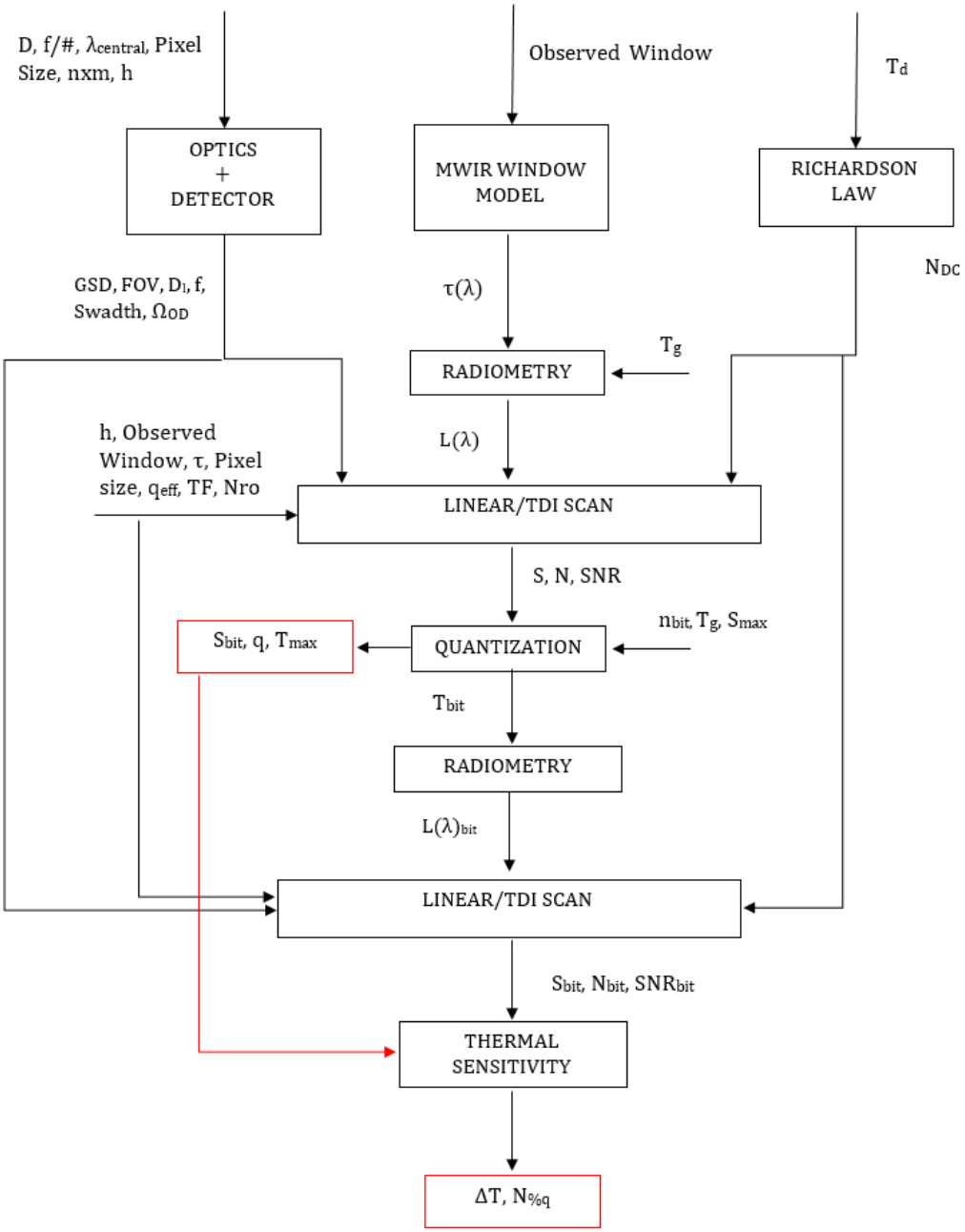

Figure 4.1: Block scheme for Linear and TDI scan simulation software

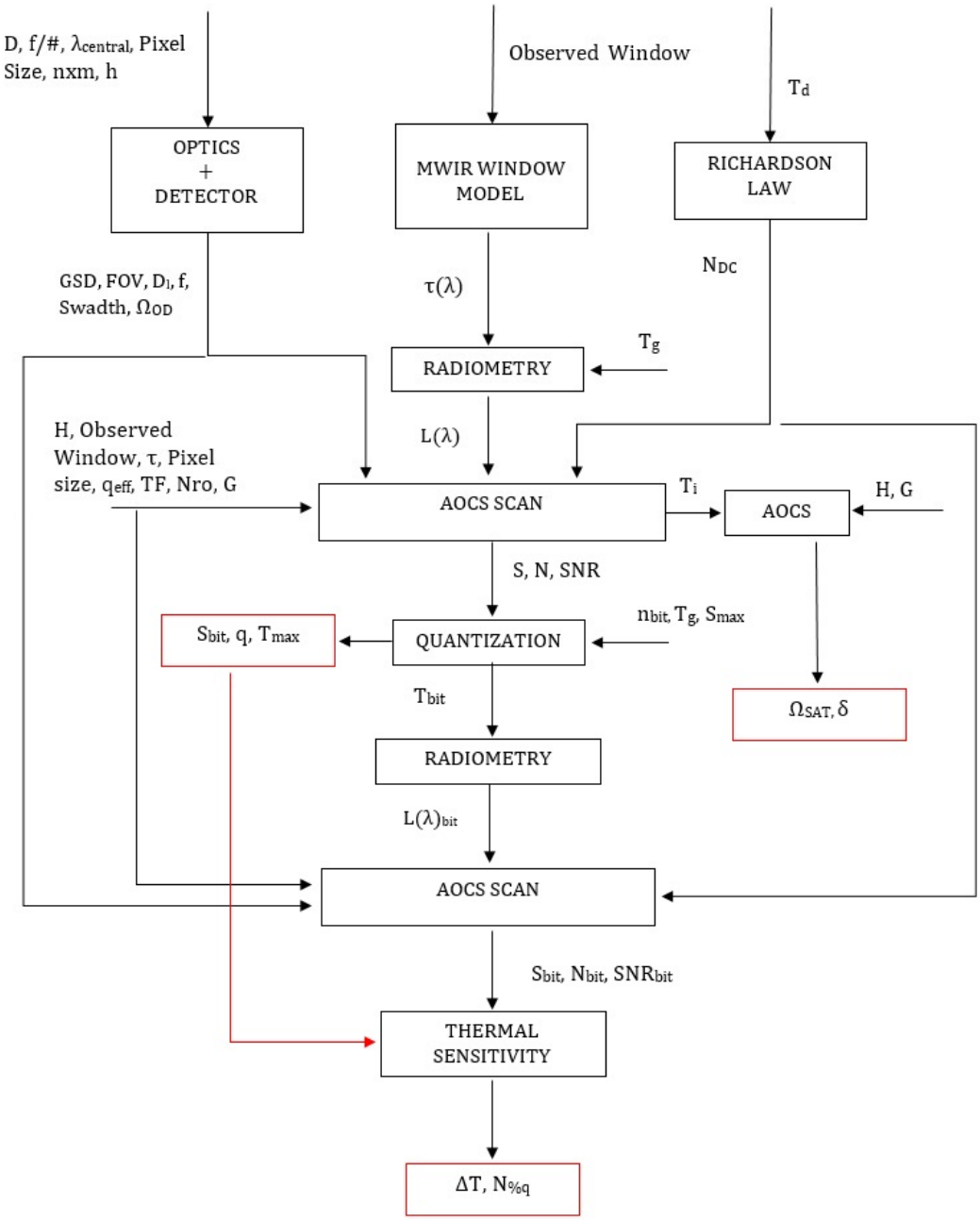

Figure 4.2: Block scheme for AOCS scan simulation software

Table 4.1: Parametric Study Input and Output

	Input	**Symbol**	**Output**	**Symbol**
Camera	Pupil Diameter	D	Focal Distance	f
	$f/\#$		FOV	
	Optics Transmission	τ	Swadth	SW
	Linear Filter Transmission	TF		
	Observed Bandwidth	WL		
Detector	Pixel size	ps	Dark Current noise	N_{DC}
	Array dimension (nxm)		Diffraction Limit	D_l
	Read Out Noise	N_{RO}		
	Detector Temperature	T_d		
	Quantum Efficiency	q_{eff}		
	Well Capacity	S_{max}		
	Digital Resolution	n_{bit}		
Orbit	Orbit Altitude	H	Satellite velocity	V_{sat}
			Integration Time	T_i
Radiometry	Ground Temperature	T_g	Thermal Radiance	I_{pupil}
Global			GSD at Nadir	GSD
			Beam Solid Angle	Ω_{SO}
			Collected power	P
			Signal	S
			SNR	
			Min. Detectable Temp.	T_{min}
			Max. Detectable Temp.	T_{max}
			Thermal Sensitivity	ΔT
			AOCS Time Gain	G
			AOCS rot. vel.	Ω_{sat}

4.2 Instrument Characteristic Prediction

In Tab.7.2 and Tab.7.3 are reported the results of four simulations. For each of the two configurations the performances have been evaluated at two different values of altitudes, respectively 400km and 800km.
The simulations are performed for a range of ground temperatures. Hence, two extreme results have been reported where required.

Table 4.2: Simulation example #1, results

Input	**Value**	**Output**	**Results H=400km**	**Results H=800km**
D	50 mm	f	125 mm	=
$f/\#$	2.50	FOV	4.40 deg	=
τ	0.93	SW	30.72 km	61.44 km
TF	0.80			
WL	(3.00 to 5.00) μm			
ps	15 μm	N_{DC}	8.99 10^{-8} e^-/s	=
n x m	640x512 InSb	D_l	24 μm	=
N_{RO}	850 e^-			
T_d	80 K			
q_{eff}	0.70			
S_{max}	7 10^{-6} e^-			
n_{bit}	10			
H	400 & 800km	V_{sat}	7.22 km/s	6.62 km/s
T_g	(220 to 345) K	I_{pupil}	(0.012 to 2.805) W/(m^2 sr)	=
		GSD	48 m	96 m
		Ω_{SO}	0.4 arcmin	=
		P	(0.03 to 7.38)10^{-11} W	=
		Linear		
		T_i	7 ms	15 ms
		S	(2 to 553)10^4 e^-	(5 to 1204)10^4 e^-
		SNR	(9 to 1581)	(14 to 2372)
		T_{min}	260 K	255 K
		T_{max}	341 K	324 K
		ΔT	0.45@290 K	0.30@290 K
		$N_{\%q}$	114%	75%
		TDI		
		T_i	3.4 s	7.4 s
		S	(1 to 283)10^7 e^-	(3 to 616)10^7 e^-
		SNR	(209 to 35765)	(327 to 53670)
		T_{min}	<220 K	<220
		T_{max}	<220 K	<220
		ΔT	0.30@290 K	0.30@290 K
		$N_{\%q}$	0.22%	0.15%
		AOCS		
		G	2.5	=
		Ω_{sat}	1.2 10^{-4} rad/s	=
		δ	5.70 10^{-5} deg	1.25 10^{-4} deg
		T_i	17 ms	36 ms
		S	(6 to 1381)10^4 e^-	(13 to 3011)10^4 e^-
		SNR	(15 to 2545)	(23 to 3782)
		T_{min}	253 K	245 K
		T_{max}	319 K	298 K
		ΔT	0.30@290 K	0.30@290 K
		$N_{\%q}$	70%	47%

Table 4.3: Simulation example #2, results

Input	**Value**	**Output**	**Results H=400km**	**Results H=800km**
D	20 mm	f	100 mm	=
$f/\#$	5.0	FOV	5.50 deg	=
τ	0.93	SW	38.40 km	76.80 km
TF	0.80			
WL	(3.00 to 5.00) μm			
ps	15 μm	N_{DC}	8.99 10^{-8} e^-/s	=
n x m	640x512 InSb	D_l	49 μm	=
N_{RO}	850 e^-			
T_d	80 K			
q_{eff}	0.70			
S_{max}	7 10^{-6} e^-			
n_{bit}	8			
H	400 & 800km	V_{sat}	7.22 km/s	6.62 km/s
T_g	(220 to 345) K	I_{pupil}	(0.012 to 2.805) W/(m^2 sr)	=
		GSD	60 m	120 m
		Ω_{SO}	0.5 arcmin	=
		P	(0.03 to 7.38)10^{-11} W	=
		Linear		
		T_i	8 ms	18 ms
		S	(0.7 to 172)10^4 e^-	(2 to 376)10^4 e^-
		SNR	(3 to 548)	(4 to 826)
		T_{min}	292 K	282 K
		T_{max}	>345 K	>345 K
		ΔT	1.24@290 K	1.24@290 K
		$N_{\%q}$	89%	59%
		TDI		
		T_i	4.3 s	9.3 s
		S	(4 to 884)10^6 e^-	(8 to 1927)10^6 e^-
		SNR	(59 to 12407)	(93 to 18690)
		T_{min}	227 K	<220
		T_{max}	228 K	<220
		ΔT	1.24@290 K	1.24@290 K
		$N_{\%q}$	0.17%	0.12%
		AOCS		
		G	2.5	=
		Ω_{sat}	1.5 10^{-4} rad/s	=
		δ	0.9 10^{-4} deg	=
		T_i	20 ms	45 ms
		S	(2 to 431)10^4 e^-	(4 to 941)10^4 e^-
		SNR	(4 to 887)	(7 to 1320)
		T_{min}	280 K	271 K
		T_{max}	>345 K	332 K
		ΔT	1.24@290 K	1.24@290 K
		$N_{\%q}$	55%	37%

First of all, the obtained results confirmed the predicted behaviors with the orbit altitude. A higher orbit allows for higher SNR. Despite also the GSD increases it can be contained in values close to 100m. Moreover, in view of the higher amount of collected Signal, noises will less affect the thermal sensitivity ($<N_{\%q}$). Then, the dictated orbit will not represent a hard obstacle for the mission design.

About the optics, the reported simulations are based on substantially different combinations of pupil aperture and $f/\#$, while the pixel size is fixed at the minimum possible value. These two combinations, in fact, lead to similar values of GSD while an appreciable difference can be found in the SNR.
The combination of a relatively high aperture with a small $f/\#$ appears more performant than the opposite case, thanks to the higher collected Signal [1].
Unfortunately, a problem appears for elevated $f/\#$. High $f/\#$ values involve high Diffraction Limit (in the example #2 it is equal to 49μm). Considering the use of 15μm pixel, and a central wavelength of 4μm, $f/\#$ should not be higher than 3.

Concerning the scan method, the simulations are based on a standard 640x512 FPA. The simple Linear scan lead anyhow to good values of SNR in a very appreciable range of temperatures, especially in the first case (260 to 341 K).
Must be remembered that the best conditions for the observation are assumed. Then, despite the optimistic results, SNR improvement will be necessary to ensure the instrument operational.

The simulations put in evidence problems in use TDI and AOCS scan: the TDI scan appears to be oversized and the AOCS unfeasible.
The use of TDI scan saturates the pixel at very low temperatures (<220K), making the huge SNR (in the order of 10^4) unusable. In the other hand, the use of AOCS allows to regulate the SNR improvement but, its use should require extreme (and unattainable) attitude control performances (starting tilt angle inthe order of 10^{-4}).
For those reasons, the use of these methods must be explored more into deep in the design. The easiest solution could be the use of smaller FPA or the reduction of pixel rows in TDI scan. Reach a good use of AOCS scan intead seems to required much more effort (but it is not impossible). Issue to be faced in the next stages of the project.

Finally, the digital resolution must be adjusted in retrospect, basing on the $N_{\%q}$ value, but the upper limit can be assumed to be between 8 and 10 bit.

[1] Remind that these examples are purely indicative, all the combinations are valid.

Chapter 5

Conclusions

5.1 Real Instruments Simulation

In view of the performed parametric studies and the preliminary simulations, two instruments have been selected as possible candidates to be mounted on the 3U CubeSat (Fig.5.1).
The first and most promising is the *SemiConductor Devices* (SCD) Kinglet. Kinglet is based on SCD's state-of-the-art XBn (InAsSb) technology which demonstrates high performance at 150K FPA operating temperature. The product was developed in response to market demand for reduced SWaP (Size, Weight, and Power) and for increased reliability [18].
The second one is Neutrino from *FLIR*. The Neutrino is the ideal solution when SWaP design constraints, cost, and performance are needed. Featuring the latest technological advancements, The Neutrino is FLIR's smallest and lightest cooled camera core and incorporates the industry's most advanced image processing at the lowest cost and with the easiest integration of any MWIR System [19].

(a) **(b)**

Figure 5.1: (a) SCD's Kinglet [18] & (b) FLIR's Neutrino [19]

Table 5.1: Kinglet and Neutrino cameras performance comparison [1]

DATA	**KINGLET**	**NEUTRINO**
	INPUT	
D	40 mm	=
$f/\#$	2.50	=
τ	0.93	=
TF	0.80	=
WL	(3.00 to 5.00) μm	(3.60 to 4.20) μm
ps	15 μm	=
n x m	640x512 XBn(InAsSb)	640x512 InSb
$N_{RO}*$	850 e^-	=
T_d	150 K	80K
$q_{eff}*$	0.70	=
S_{max}	3 $10^{-6}\,e^-$	7 $10^{-6}\,e^-$
n_{bit}	8	=
H	600km	=
T_g	(220 to 345) K	=
	OUTPUT	
f	100 mm	=
FOV	2.50	=
SW	57.60km	=
N_{DC}	$1.93\,10^6\,e^-$/s	$8.99\,10^8\,e^-$/s
D_l	24 μm	=
GSD	90	=
T_i	0.01302s	=
S	(8.9 to 275) $10^4\,e^-$	(36 to 640) $10^4\,e^-$
SNR	(100 to 1470)	(100 to 1470)
T_{min}	254K	255K
T_{max}	332K	327K
ΔT	1.14@295K	1.22@290K
$N_{q\%}$	20%	20%

[1] Values of Input variables marked with * have been assumed by the user.

In Tab.5.1 are reported the results of the simulations based on a common optical system, an orbit of $H = 600km$, and both the two camera datasheet found on the respective company websites [2].

In fact, the two cameras differ only for the Observed Bandwidth (more narrow for Kinglet) and the Detector Temperature (lower for Neutrino). For that reason, all the output related to the geometry of the system (GSD, SW, T_i, etc..) are equal for the two instruments.

What is surprising is that also the obtained SNR, range of detectable temperatures, and Temperature Resolutions are all very close for the two instruments. The only big difference is in the cooling system. Both mounting a cryo-cooler Stirling engine, the two detectors operate at very different temperatures. Kinglet is more compact and energy safer, asking for 2 to 3.5 W [3] instead of the 5W required by Neutrino [4]. This properties allow the easy use and arrangement of the Kinglet camera on a 3U CubeSat. Neutrino is bigger than Kinglet, requiring more than 1U of space, and with a hardly sustainable energy consume (Tab.5.2).

In conclusion, the best candidate seems to be the *SCD*'s Kinglet camera. But the use of the *FLIR*'s Neutrino has not been precluded.

Table 5.2: Kinglet and Neutrino cameras size comparison

DATA	**KINGLET**	**NEUTRINO**
Size	80x38x60mm	127x51x74mm
Weight	<300g	<450g
Input Power (S.S.)	<3.5W	<5W

5.2 Mission Feasibility

The continuously increasing in small satellites (especially CubeSat) employment, requires a continue progression in instruments miniaturization. The development of the new technologies in the Infrared observation field leads to obtaining instruments able to satisfy the always more restrictive SWaP requirements.

Concerning the MWIR imaging, at the end of this work, it is possible to assert that Earth observation through this atmospheric window is feasible for a 3U CubeSat flying in a LEO. The required technology is now available and accessible for research applications.

Nevertheless, there are still some open questions, such as the identification of the best SNR improvement method or the cooling issue. Moreover, since it has been a preliminary study, it will be necessary to elaborate more detailed models, and relax more hypothesis as possible. These challenges will be addressed in the next stages of the project by students and professors of the *Université de Liège* and *CSL*.

[2] Only Linear Scan has been considered.
[3] Three different cryo-systems, with three different power consumptions, are proposed for Kinglet.
[4] The reported values are related to steady-state operation conditions.

Appendix A:

Model Codes

MWIR model code, File name: MWIR_window.m

```
function[st]=MWIR_window(WL)
% TRANSMISSION MWIR WINDOW MODEL
% Input: observed bandwidth wavelengths (um)
% Output: atmospheric transmission coefficient
for g=1:length(WL)
    if WL(g)≥3 && WL(g)≤3.4
        m=0.45/0.4;
        q=-3*m;
        st(1,g)=WL(g)*m+q;
    elseif WL(g)>3.4 && WL(g)<4.2
        st(1,g)=0.75;
    elseif WL(g)≥4.2 && WL(g)≤4.4
        st(1,g)=0;
    elseif WL(g)>4.4 && WL(g)≤5
        m=-0.55/0.62;
        q=5.2*m;
        st(1,g)=WL(g)*m-q;
    end
end
```

Detector's Dark Current model, in that case the curve for InSb has been implemented. File name: DarkCurrentInSb.m

```
function[DC,I]=DarkCurrentInSb(ps,Td)
% INPUT:
    % ps=pixel size (um)
    % Td=detector temperature (K)
 %OUTPUT
    % DC=Dark current (e/s)
    % I = Dark current (A)
k=1.38064852e-23;       %Boltzmann constant (J/K)
dE=0.16*1.6022e-19;     %Activation Energy (J)
C=1.2e6;                %(A/(m^2 K^2)
Qe=1.6e-19;             %Electron Charge (C)
Ad=(ps./(10^6)).^2;     %detector area (m2)
I=Ad.*C.*Td.^2.*exp(-dE./(k.*Td));
DC=I./(Qe);
end
```

Optical system and Detector model code, File name: optic.m

```
function [GSD,FOV1,FOV2,iFOV,DL,v,...
            FPS1,FPS2,Pl_s,SW,Om_fp]=optic(z,f_numb,l,ps,n,m,h,y)
%% DESCRIPTION
%This function must be used to compute all the geometric parameters derived
%from optics and sensor dimensions
%% PARAMETERS
%INPUT:
    % z:
            % 1: f=focal distance (mm)
            % 2: D=Pupil Diameter (mm)
    % f_numb=f-number
    % l=central wavelength (um)
    % ps=pixel size (um)
    % n=pixel number on dimension 1
    % m=pixel number on dimension 2
    % h=orbit altitude  (km)
%OUTPUT:
    % GSD=Ground Sample Distance (m)
    % FOV1=Field of View on dimension 1 (deg)
    % FOV2=Field of View on dimension 2 (deg)
    % iFOV=Istantaneous Field of View (rad)
    % DL=Diffraction Limit (um)
    % v:
            % 1: D=Pupil Diameter (mm)
            % 2: f=focal distance (mm)
    % FPS1=Focal Plane Size on dimension 1 (mm)
    % FPS2=Focal Plane Size on dimension 2 (mm)
    % Pl_s=Plate Scale (deg/mm)
    % SW=swath width (km)
    % Om_fp=Solid Angle between Detector and Pupil (sr)
%% COMPUTATIONS
DL=1.22*2*f_numb*l;
if DL>ps
    fprintf('WARNING: the pixel size is exceeding the diffraction limit \n')
end
if y==1
    f=z;
    D=f./f_numb;
    v=D;
elseif y==2
    D=z;
    f=D.*f_numb;
    v=f;
end
alpha=ps./f*10^(-3);
iFOV=atan(alpha);
FOV1=iFOV.*n/pi*180;
FOV2=iFOV.*m/pi*180;
GSD=h*1000.*tan(alpha);
FPS1=ps.*n/1000;
FPS2=ps.*m/1000;
Pl_s=180./(pi.*f);
SW=GSD.*n/1000;
Om_fp=pi./(4.*f_numb.^2);
end
```

Radiometric Budget model, File name: facet2.m

```
function [B_e,Lsri,Lep,Lsrp,Lu,Lp]=facet2( WL,T_e,st)
%% FUNCTION DESCRIPTION
%This function must be used to compute both the sun-reflected and ...
    re-emitted radiation which reach the pupil
%of the on-board otpics.
%% PARAMETERS DESCRIPTION
%INPUT:
    % WL= observed bandwidth wavelengths vector (um)
    % T_e=ground temperature vector (K)
    % st=Atmosphere MWIR transmission coefficient
%OUTPUT:
    % B_e=emitted radiance by grey body ground  (W/(m2 sr m))
    % Lsri=solar radiance reflected from the ground  (W/(m2 sr m))
    % Lep=emitted radiance after atmosphere absorption (W/(m2 sr m))
    % Lsrp=reflected radiance after atmosphere absorption  (W/(m2 sr m))
    % Lu=total radiance coming from the ground (W/(m2 sr m))
    % Lp=total radiance after atmosphere absorption  (W/(m2 sr m))
%% CONSTANTS
h=6.62607004e-34;       %Planck constant (J s)
c=3e08;                 %Speed of light (m/s)
k=1.38064852e-23;       %Boltzmann constant (J/K)
T_s=5900;               %Sun Temperature(K)
l=WL*10^(-6);           %Wavelengtg (m)
r=0.2;                  %Ground reflectivity coefficient
eps=0.8;                %Ground Grey body emissivity
%% SUN RADIATION
%Radiation coming from Sun before enter in the atmosphere (Es_exo)
%Hp: Black Body Emitter, T=5900K
%Solid angle Sun-Earth (sr)
OM=6.8e-05;
%Solar radiance (W/(m2 m))
Ls_exo=(2*h*c^2)./l.^5./(exp(h*c./(l.*k*T_s))-1)*OM;
%Solar radiance at the ground (W/(m2 m))
Ls=Ls_exo.*st;
%Reflected solar radiance from an hemisphere (W/(m2 sr m))
Lsri=Ls*r/(2*pi);
%% TOTAL EMISSION
%Radiation leaving the surface (emitted/reflected)
%Hp: Grey Body, T=255K ,eps=0.8; Lambertian source
for i=1:length(T_e)
    %Face emitted radiance per wavelenght (W/(m2 sr m))
    B_e(i,:)=(2*h*c^2)./l.^5./(exp(h*c./(l.*k*T_e(i)))-1)*eps;
    %Multiplying to "st" the radiance exiting by the atmosphere is computed
    %Exiting re-emitted radiance (W/m2 sr m)
    Lep(i,:)=B_e(i,:).*st;
    %Exiting refleceted sun radiance (W/m2 sr m)
    Lsrp=Lsri.*st;
    %Total radiance coming from the ground (W/(m2 sr m))
    Lu(i,:)=B_e(i,:)+Lsri;
    %Total radiance per wavelength at the pupil (W/(m2 sr m))
    Lp(i,:)=Lep(i,:)+Lsrp;
end
end
```

Appendix B:

SNR & Quantization Codes

Linear Scan and TDI SNR computation. The AOCS is similar, but Integration Time is computed from AOCS Gain. File name: SNR_comp.m

```
function [S,Sd,N,SNR,SNRd,Ti,Tid,V_sat,...
            Ls,P]=SNR_comp(H,WL,GSD,Lp,t,ps,q_eff,TF,DC,Nro,Om_fp,M)
%% DESCRIPTION
%This function must be used for the computation of the SNR based on the
%sensor datas, the optics and the spacecraft orbit
%% PARAMETERS
%INPUT
    % H=orbit altitude (km)
    % WL=wavelength band (um)
    % GSD= Ground Sampling Distance (m)
    % Lp=radiance at the pupil (W/(m2 sr m))
    % t=instrument trasmition coefficient
    % ps=pixel size (um)
    % BW=band width (um)
    % q_eff=quantum efficiency
    % TF=Transmition of the linear filter
    % DC=Dark current (e/s)
    % Nro=Read Out Noise (e)
    % Om_fp=solid angle between detector and pupil (sr)
    % M=TDI pixel rows
%OUTPUT
    % S= Linear Scan Signal (e)
    % Sd=TDI Signal (e)
    % N=Total Noise (e)
    % SNR=Linear Scan Signal to Noise Ratio
    % SNRd=TDI Signal to Noise Ratio
    % Ti=Integration Time (s)
    % Tid=TDI Integration Time (s)
    % V_sat=satellite velocity wrt ground (km/s)
    % Ls=total radiance collected by the pupil (W/(m2 sr))
    % P=Power that reach one pixel (W)
%CONSTANT
Re=6371;            %Earth radius (km)
mu=398600.4418;     %Earth Gravitational Parameter (km3/s2)
h=6.62607004e-34;   %Planck constant (J s)
c=3e08;             %Speed of light (m/s)
%%
ps=ps*10^-6;            %pixel size (m)
Ad=ps.^2;               %detector area (m2)
l=WL*10^-6;             %bandwidth wavelengths vector (m)
L=(min(l)+max(l))/2;    %central wavelength (m)
a=Re+H;                 %Orbit radius (km)
To=2*pi*sqrt(a^3/mu);   %Orbit period (s)
V_sat=2*pi*Re/To;       %Spacecraft velocity wrt ground (km/s)
Ti=GSD/V_sat*0.001;     %Linear Scan Integration time (s)

[p,q]=size(Lp);
for i=1:p
%Radiance at pupil (W/m2 sr)
Ls(i)=trapz(l,Lp(i,:));
%Power at the pixel (W)
```

```
P(i,:)=Ls(i)*Om_fp*Ad*t;
%Photon flux to pixel (e/s)
I(i,:)=P(i,:).*L*q_eff/(h*c);
%Linear Scan Signal (e)
S(:,i)=I(i,:).*Ti*TF;
%Signal Noise (e)
Ns(:,i)=sqrt(S(:,i));
%Dark Current Noise (e)
Ndc=sqrt(DC.*Ti);
%Total Noise (e)
N(:,i)=sqrt(Ns(:,i).^2.+Ndc.^2.+Nro^2);
%Linear Scan Signal to Noise Ratio
SNR(:,i)=S(:,i)./N(:,i);
%TDI integration time and SNR
if M>1
      Tid=Ti*M;
    SNRd(:,i)=SNR(:,i)*sqrt(M);
    Sd(:,i)=S(:,i)*M;
else
    Tid=Ti;
    SNRd=SNR;
end
end
end
```

Digital quantization. File name: pixel_power2.m

```
function[Sbit,Tbit,q,DT,S2,Tmax,u]=pixel_power2(S,T,nbit,Ssat)
%% PARAMETERS
% INPUT
    % T= ground temperature vector (K)
    % S= signal vector correspond to the ground temperatures (e-)
    % nbit=digital resolution
    % Ssat=well capacity (e-)
%OUTPUT
    % Sbit = quantized signal scale (e-)
    % Tbit = quantized temperature scale (K)
    % DT = quantization temperature step (K)
    % S2 = signal from Tbit (e-)
    % Tmax = Saturation Temperature (K)
    % u = DT index
%% COMPUTATIONS
M=2^nbit;
q=(max(S))/M;
%Inverse law polynomial
f=ceil(max(S)/q);
Sbit=[0:q:f*q];
Pol1=pchip(S,T);
Tbit=ppval(Pol1,Sbit);
%Direct law polynomial (for check)
Pol2=pchip(T,S);
S2=ppval(Pol2,T);
%Saturation temperature
Tmax=ppval(Pol1,0.9*Ssat);
Tmax=round(Tmax,3,'significant');
%Thermal sensitivity
u=ceil(length(Tbit)/6);
dT(1)=abs(Tbit(u+1)-Tbit(u));
dT(2)=abs(Tbit(u-1)-Tbit(u));
dT(3)=abs(Tbit(u+1)-Tbit(u-1))/2;
DT=round(mean(dT),2,'decimal');
end
```

Appendix C:

Simulation Code

Global instrument simulation. File name: Instrument_sym.m

```
%% DATA
%Optics
D=40;                           %Pupil Diameter
f_numb=3;                       %f#
ps=15;                          %pixel size (um)
n=640;                          %number of pixel on dimension 1
m=1;                            %number of pixel on dimension 2
M=512;                          %number of TDI pixel
WL=linspace(3,5,10000);         %observed wavelength band (um)
wl=(min(WL)+max(WL))/2;         %wavelength (um)
h=400;                          %orbit altitude (km)
T_e=linspace(220,345,200);      %ground temperature (K)
%Detector
t=0.93;                         %instrument trasmition coefficient
q_eff=0.7;                      %quantum efficiency
TF=0.8;                         %Transmition of the linear filter
Td=80;                          %Detector Temperature (K)
Nro= 850;                       %Read Out noise (e-)
nbit=8;                         %Digital Resolution
Ssat=7e06;                      %Pixel capacity (e-)
G=2.5;                          %AOCS Gain

%% COMPUTATION
%Radiometric budget and instrument models
[st]=MWIR_window(WL);
[Le,Lsr,Lep,Lsrp,Lu,Lp]=facet2(WL,T_e,st);
[GSD,FOV1,FOV2,iFOV,DL,f,FPS1,FPS2,...
            Pl_s,SW,Om_fp]=optic(D,f_numb,wl,ps,n,m,h,2);
[DC]=DarkCurrentInSb(ps,Td);
[S,Sd,N,SNR,SNRd,Ti,Tid,V_sat,Ls,P]=SNR_comp(h,WL,GSD,...
            Lep,t,ps,q_eff,TF,DC,Nro,Om_fp,M);
%%
%Linear Scan quantization
[Sbit,Tbit,q,dt,S1,Tmax,u]=pixel_power2(S,T_e,nbit,Ssat);
[Leb,Lsrb,Lepb,Lsrpb,Lub,Lpb]=facet2(WL,Tbit,st);
[Sb,Sdb,Nb,SNRb,SNRdb,Tib,Tidb,V_sat,Lsb,Pb]=SNR_comp(h,WL,GSD,...
            Lepb,t,ps,q_eff,TF,DC,Nro,Om_fp,M);
    %Thermal sensitivity determination
    diff=mean(2*Nb/q*100);
    if diff>100
        DT=ceil(diff/100+1)*dt;
    elseif diff≤100
        DT=2*dt;
    end
%TDI quantization
[Sbitd,Tbitd,qd,dtd,S1d,Tmaxd,u]=pixel_power2(Sd,T_e,nbit,Ssat);
[Lebd,Lsrbd,Lepbd,Lsrpbd,Lubd,Lpbd]=facet2(WL,Tbitd,st);
[Sbd,Sdbd,Nbd,SNRbd,SNRdbd,Tibd,Tidbd,V_sat,...
        Lsbd,Pbd]=SNR_comp(h,WL,GSD,Lepbd,t,ps,q_eff,...
            TF,DC,Nro,Om_fp,M);
    %Thermal sensitivity determination
    diffd=mean(2*Nbd/qd*100);
```

```
    if diffd>100
        DTd=ceil(diffd/100+1)*dtd;
    elseif diffd≤100
        DTd=2*dtd;
    end
%AOCS quantization
[Sa,Na,SNRa,Tia,Tiaa,Lsa,Pa]=SNR_comp_AOCS(h,WL,GSD,...
            Lep,t,ps,q_eff,TF,DC,Nro,Om_fp,G);
[Ti_c,OM,tilt,Om_sat]=AOCS(h,Ti,G);
[Sbita,Tbita,qa,dta,S1a,Tmaxa,u]=pixel_power2(Sa,T_e,nbit,Ssat);
[Leba,Lsrba,Lepba,Lsrpba,Luba,Lpba]=facet2(WL,Tbita,st);
[Sba,Nba,SNRba,Tiba,Tibaa,Lsba,Pba]=SNR_comp_AOCS(h,WL,GSD,...
            Lepba,t,ps,q_eff,TF,DC,Nro,Om_fp,G);
diffa=mean(2*Nba/qa*100);
    %Thermal sensitivity determination
    if diffa>100
        DTa=ceil(diffa/100+1)*dta;
    elseif diffa≤100
        DTa=2*dta;
    end

%% PLOTS
%Only example for linear scan is reported
%Discretized signal scale
figure(1)
stairs([Sbit-q/2,Sbit(end)+q/2],[Tbit,Tbit(end)])
hold on
plot(Sbit,Tbit,'ok')
hold off
ylabel('Ground Temperature (K)')
xlabel('Signal (e^-)')
grid on
for i=1:length(Sbit)
    hold on
    plot([Sbit(i)-Nb(i),Sbit(i)+Nb(i)],[Tbit(i),Tbit(i)],'*r',...
        [Sbit(i)-Nb(i),Sbit(i)+Nb(i)],[Tbit(i),Tbit(i)],...
            'r','LineWidth',1)
    hold off
end

title(sprintf('Thermal resolution in %dbit \n T_{min}=%3.2fK,  ...
    T_{max}=%3.2fK, Ti=%2.3fs \n Td=%3.2fK,  DT=%1.2f@%3.0fK,  Nq%% %2.2f ...
    %%',nbit,260,Tmax,Ti,Td,DT,Tbit(u),diff))
legend('Signal','Central temperature','Noise','Location','northwest')
```

Bibliography

[1] NASA. Aquarius: spacecraft and mission, 2011.

[2] Planetary Resource. Planetary resources first spacecraft successfully deployed, testing asteroid prospecting technology on orbit. http://www.planetaryresources.com/2015/07/planetary-resources-first-spacecraft-deployed/, 2015.

[3] Planetary Resource. The arkyd 100 space telescope: a commercial space telescope within reach of the private citizen. https://web.archive.org/web/20140814194054/http://www.planetaryresources.com/technology/leo-space-telescope/, 2013.

[4] NASA/JPL Thomas S. Pagano. Cubesat infrared atmospheric sounder (ciras). https://www.jpl.nasa.gov/cubesat/missions/ciras.php.

[5] Herbert J. Kramer. Tet-1 (technology experiment carrier-1). https://directory.eoportal.org/web/eoportal/satellite-missions/t/tet-1.

[6] Malkmus W. Random lorentz band model with exponential-tailed s line intensity distribution function. *J. Opt. Soc. Am.The Journal of the Optical Society of America*, (57):323–329, 1967.

[7] B. García-Lorenzo, J.A. Castro-Almazána, A. Eff-Darwichc, C. Muñoz-Tuñóna, N. Pinilla-Alonsod, J.M. Rodríguez-Espinosaa, and I. Romeroe. Precipitable water vapour content above the roque de los muchachos observatory from gps estimations. *Proceedings of SPIE - The International Society for Optical Engineering*, 2009.

[8] Michael K. Griffin, Hsiao hua K. Burke, and John P. Kerekes. Understanding radiative transfer in the midwave infrared, a precursor to full spectrum atmospheric compensation. In Paul E. Lewis Sylvia S. Shen, editor, *Algorithms and Technologies for Multispectral, Hyperspectral, and Ultraspectral Imagery X*, volume 5425, pages 348–356. SPIE, Bellingham, WA, 2004.

[9] Michael T. Eismann. *Hyperspectral Remote Sensing*. SPIE, Bellingham, Washington USA, 2012.

[10] James M. Palmer and Barbara G. Grant. *The Art of Radiometry*. SPIE, Bellingham, Washington USA, 2009.

[11] U.S. Government Printing Office NIST SP811. *Guide for the Use of the International System of Units (SI)*, 1995.

[12] Baldridge, A. M., S.J. Hook, C.I. Grove, and G. Rivera. The aster spectral library version 2.0. remote sensing of environment. volume 113, pages 711–715. 2009.

[13] John W. Salisbury and Dana M. D'Aria. Emissivity of terrestrial materials in the 3-5 µm atmospheric window. *Remote Sens. Environ.*, (47):345–361, 1994.

[14] M. Taccola, D. De Wilde, S. Grabarnik, F. Michel C. De Clercq, and W. Moelans G. Taglioni. Miniaturized hyperspectral imagers for cubesats. Pestana Conference Centre – Funchal, Madeira - Portugal, 31 May — 4 June 2010.

[15] Nathanael Assefa. 3 principles of super-lensing: Overcoming the diffraction limit. *Catalyst*, October 15, 2016.

[16] *Future U.S. Workforce for Geospatial Intelligence*. The National Academies Press, 2013.

[17] Yakov Bulayev for Hamamatsu Corporation. Tdi imaging: an efficient aoi and axi tool. `http://www.hamamatsu.com/eu/en/community/optical_sensors/articles/tdi_imaging_for_aoi_axi_ndt/index.html`, March 2012.

[18] SemiConductor Devices. Kinglet 640, 15µm. `http://www.scd.co.il/KINGLET-640-15`.

[19] FLIR. Flir neutrino. `http://www.flir.com/cores/display/?id=60562`.